

April 2014

# Bio-electromagnetic Instrumentation Problems Related to the Human Body

Chan Young Choi

*Worcester Polytechnic Institute*

Charvi Tyagi

*Worcester Polytechnic Institute*

Michael Jacob Ruzzi

*Worcester Polytechnic Institute*

Nicholas Patrick Muller

*Worcester Polytechnic Institute*

Follow this and additional works at: <https://digitalcommons.wpi.edu/mqp-all>

---

## Repository Citation

Choi, C. Y., Tyagi, C., Ruzzi, M. J., & Muller, N. P. (2014). *Bio-electromagnetic Instrumentation Problems Related to the Human Body*. Retrieved from <https://digitalcommons.wpi.edu/mqp-all/1247>

This Unrestricted is brought to you for free and open access by the Major Qualifying Projects at Digital WPI. It has been accepted for inclusion in Major Qualifying Projects (All Years) by an authorized administrator of Digital WPI. For more information, please contact [digitalwpi@wpi.edu](mailto:digitalwpi@wpi.edu).

# **Bio-Electromagnetic Instrumentation Problems Related to the Human Body – Osteoporosis Detection**

A Major Qualifying Project Report  
Submitted to the Faculty of the

WORCESTER POLYTECHNIC INSTITUTE



In partial fulfillment of the requirements for the  
Degree of Bachelor of Science

By:

---

Nick Muller

---

Michael Ruzzi

---

Chan Young Choi

---

Charvi Tyagi

May 2014

Approved by:

---

Prof. Sergey Makarov, Advisor  
Electrical and Computer Engineering Department

## Abstract

Long bone fractures account for approximately 10% of all non-fatal injuries in the United States. A significant portion of them are due to osteoporosis. The objective of this project is to test different methods for detecting osteoporotic bones, both theoretically and experimentally. They include:

1. Steady-state electric current sensors – electric impedance tomography
2. Infrared scattering sensors
3. Microwave sensors

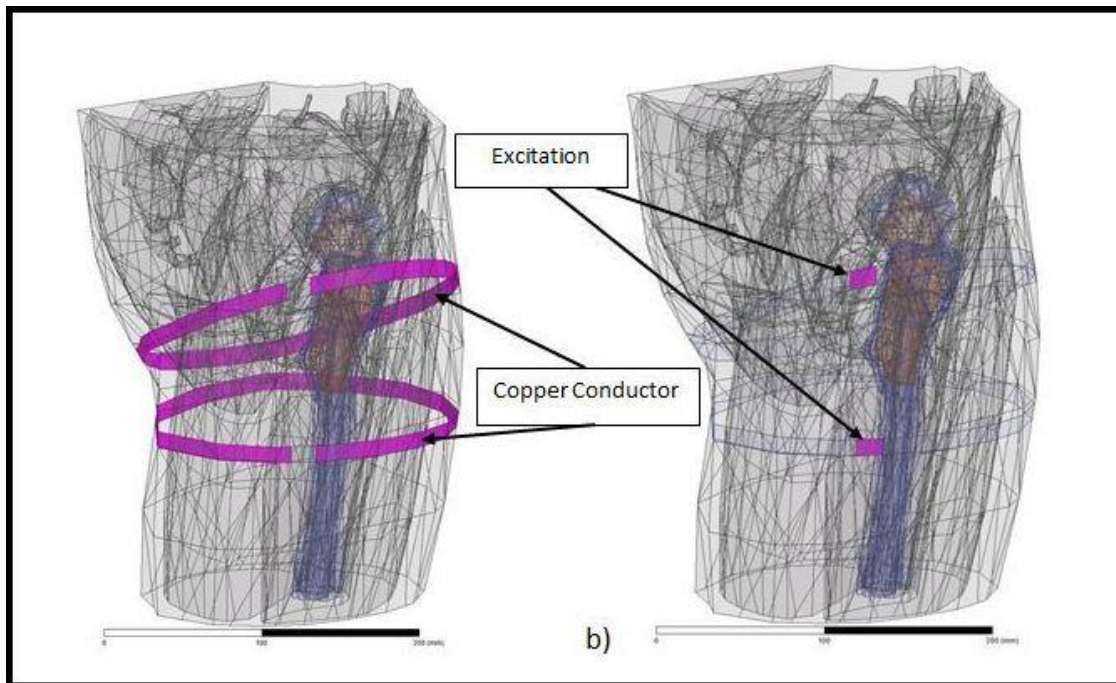


**Figure 1: Simulation of Antenna around a Human Femur [15]**

## **Acknowledgments**

We would like to deeply recognize our advisor Professor Makarov for his excellent guidance and advice throughout this project. We would also like to acknowledge all of the people who helped us throughout our MQP. First, we would like to thank Professor Steven Bitar for his excellent explanation of the Op-Amps in our Howland circuit, and Professor John McNeill for graciously allowing us to use his laboratory. We also would like to recognize Mr. Gregory Noetscher for his advice on the biomedical portion of this report, Mr. Janakinadh Yanamadala for his original theories and simulations, and Mr. Jeffery Elloian for his guidance with Ansys HFSS and all things Electromagnetic. Last, but certainly not least, we would like to extend our appreciation to Mr. Robert Boisse for helping us with the construction of our project and for his patience with our team. The problems considered in this study were inspired by Prof. Ara Nazarian of Beth Israel Deaconess Medical Center, Harvard Medical School.

## **Table of Contents**

<b>Abstract.....</b>	<b>1</b>
<b>Acknowledgments .....</b>	<b>2</b>
<b>Introduction.....</b>	<b>5</b>
<b>Problem Statement.....</b>	<b>6</b>
<b>Chapter 1 – Electrical Impedance Tomography.....</b>	<b>10</b>
I.    Simulations Review .....	10
II.   The Transconductance Amplifier.....	13
III.  Printed Circuit Board (PCB) Fabrication .....	16
III-i. Toner-Acid Backmasking Process .....	17
IV.   Device and Materials.....	18
IV-i. Basic Medical Phantom.....	18
IV-ii. Modeling Human Body Tissues.....	19
IV-iii. Conductive Plastics .....	19
V.    Electrical Impedance Tomography .....	21
VI.   Howland Circuit .....	25
VII.  Results .....	29
<b>Chapter 2 – Near Infrared Scattering Sensors.....</b>	<b>32</b>
I.    Background .....	32
II.   Simulations and Results .....	35
<b>Chapter 3 – Microwave Antenna Sensors .....</b>	<b>38</b>
I.    Background .....	38
II.   Antenna Simulations .....	39
III.  Printed Circuit Board (PCB) Fabrication .....	41
IV.   Results .....	43
IV-i. First Iteration .....	43
IV-ii. Second Iteration .....	46
<b>Conclusion .....</b>	<b>49</b>
<b>References .....</b>	<b>50</b>
<b>Appendix A – MATLAB Code to View Network Analyzer Results.....</b>	<b>52</b>
<b>Appendix B – MATLAB Code for Tissue Frequency Parameters.....</b>	<b>53</b>

## **Table of Figures**

Figure 1: Simulation of Antenna around a Human Femur .....	1
Figure 2: Osteoporotic Bone vs. Healthy Bone .....	6
Figure 3: Dielectric Constant of Different Tissues .....	7
Figure 4: Conductivity of Different Tissues .....	8
Figure 5: Human Thigh Model .....	9
Figure 6: Central Cut Simulation Results .....	10
Figure 7: Forty-Five Degree Simulation Results .....	11
Figure 8: Electrical Property change in various Frequencies .....	12
Figure 9: Operational Transconductance Amplifier Schematic.....	13
Figure 10: Multisim Simulation Circuit.....	16
Figure 11: Ultiboard Design Output .....	16
Figure 12: Finished PCB for OTA Circuit.....	17
Figure 13: Basic Phantom Device.....	18
Figure 14: Potential Semi-Conductive Materials.....	20
Figure 15: Howland Current Pump Circuit.....	25
Figure 16: Advanced Howland Circuit .....	28
Figure 17: Experimental Impedance Tomography Setup .....	29
Figure 18: DC Current Injection Oscilloscope Results.....	30
Figure 19: Infrared scattered sensors setup.....	35
Figure 20: Wrist band covered with copper foil .....	36
Figure 21: Waveform for band covered with foil .....	36
Figure 22: Set up of wrist band on the wrist.....	37
Figure 23: Waveform of IR signal across wrist.....	37
Figure 24: Ansys Simulation of Experimental Device .....	39
Figure 25: Ansys HFSS Results - Muscle Vs. Osteoporotic Bone .....	40
Figure 26: First Balun PCB Design .....	41
Figure 27: Balun and Antenna PCB Mask.....	42
Figure 28: Concept of the Balun .....	42
Figure 29: First Antenna Setup .....	43
Figure 30: Original Cylinder Results .....	44
Figure 31: Second Experimental Setup Results.....	45
Figure 32: Final Balun Design.....	46
Figure 33: Coil Antenna Setup .....	47
Figure 34: Coil Antenna Results.....	48

## Introduction

Finding an illness before it develops into a severe condition is the key to a long, healthy life. However, detecting health problems at an early stage is exceedingly difficult. In an effort to assist the diagnosis of a disease, the electrical properties of the human body have been well-researched and established over the last twenty years. Today, the electrical properties of different parts of the body can be applied to investigate illnesses and diagnose diseases. For example, the Electrocardiogram (ECG) is a device that measures the net electrical activity of the muscles in the heart. The ECG interprets the electrical currents coursing through the heart muscles during a series of heartbeats to determine the overall health of the organ. The Electroencephalogram (EEG) is a device that measures the brain waves to detect any physical anomalies or psychological conditions; it is mostly used to detect Alzheimer's disease. A fracture on the bone can be found through X-ray radiography, but it is difficult to measure the actual quality of the bone itself.

Distinguishing a healthy bone from a bone afflicted with Osteoporosis is a complicated and very expensive procedure. The following project attempts to measure the electrical activity across a set of human limbs to determine the quality of bone. Using conventional techniques to measure the properties of the bone is quite costly and requires multiple tests. The objective of this Major Qualifying Project (MQP) is to simplify the process of measuring bone quality with a focus on cost effectiveness.

The discussion in the report will include Biomedical Electric Impedance Tomography (EIT), Microwave Emission Sensors, and Near Infrared Scattering Sensors. This report will discuss how we designed, built, and evaluated these three devices in an effort to find the most useful method for diagnosing osteoporotic bone. This report will also summarize our experimental evaluations of the device and discuss the findings of these experiments as well as summarize our recommendations for further research.

## Problem Statement

Osteoporosis is a medical condition that causes the bones to become brittle and more prone to fractures due to loss of bone density. It is quickly becoming a more common ailment among an aging population. Currently, the most common methods of diagnosis are; Magnetic Resonance Imaging (MRI), X-Ray Computed Tomography (CT), or Dual-Energy X-Ray Absorptiometry (DXA). The major disadvantage with these techniques is that radiography is relatively insensitive to the disease in its early stages. This is because the bone mineral density of the patient has just started to decrease. MRI, CT, and DXA scans can start to reliably detect osteoporosis only after some substantial amount of bone loss, usually greater than 30%.

The figure below depicts the models of osteoporotic bone vs. healthy bone. For a patient with osteoporosis; the fatty bone marrow—represented by dark green—builds up over time and slowly replaces the more supportive cancellous bone—represented by light green. This results in a loss of bone mineral density, which leads to an increase in bone fragility and a greater risk of fracture.

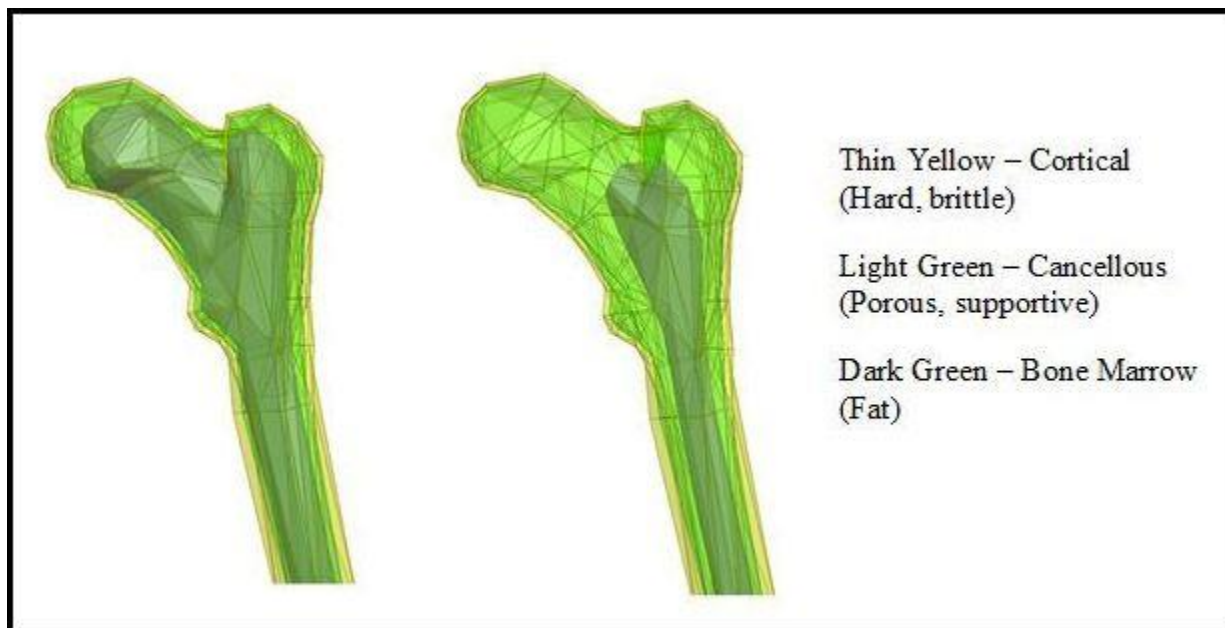
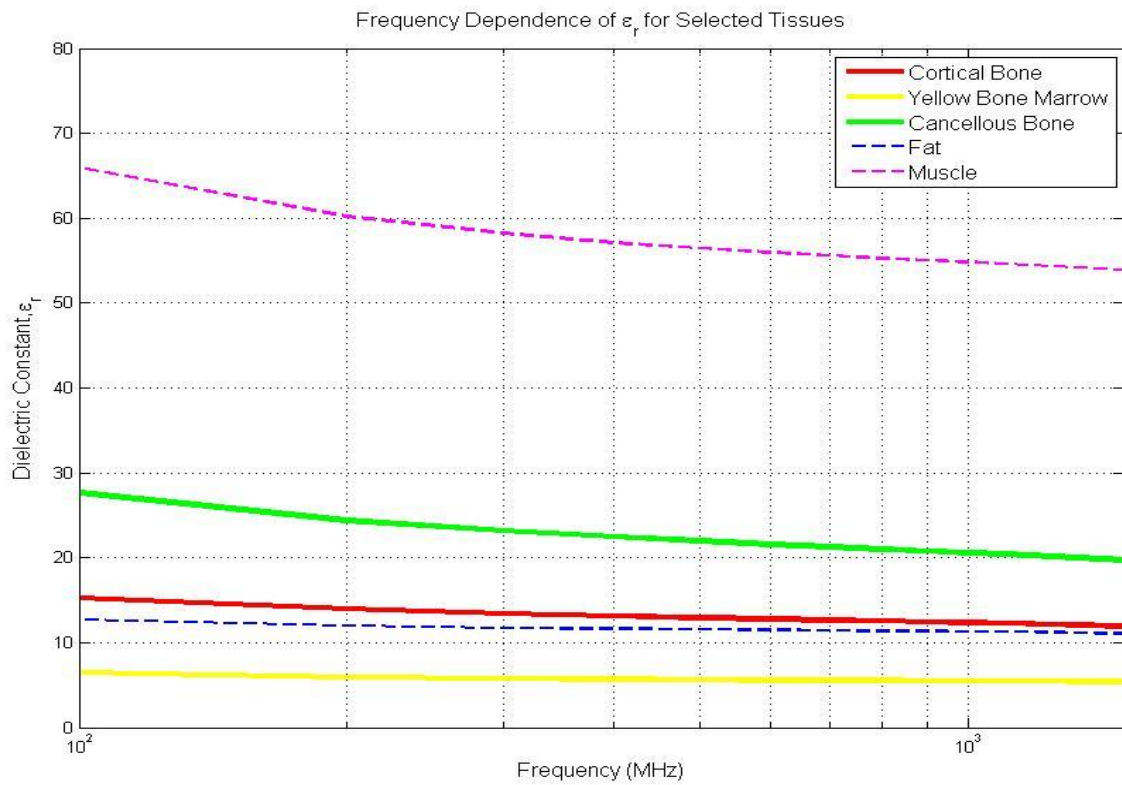


Figure 2: Osteoporotic Bone vs. Healthy Bone [18]



Figures 2 and 3 below show the dielectric constant and the conductivity for various types of bone and tissue relative to frequency. It is observed that in both instances the bone marrow (yellow), has a lower dielectric constant and a lower conductivity than the cancellous (green), and cortical (red) bone surrounding it. As a patient ages, the risk of osteoporosis increases with the loss of bone density. As more bone marrow replaces cancellous bone with time, we can hypothesize that the dielectric constant and conductivity of the overall bone will decrease by a measurable difference.



**Figure 3: Dielectric Constant of Different Tissues [9], [18]**

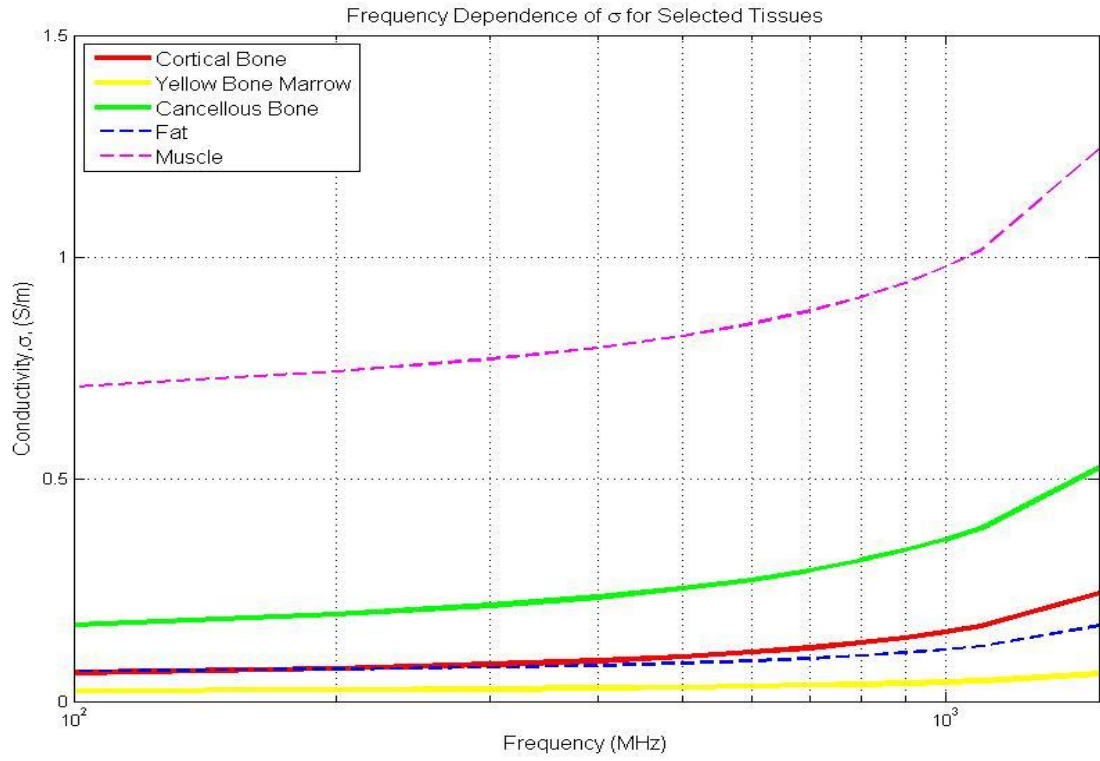


**Figure 4: Conductivity of Different Tissues [9], [18]**

However, detecting this difference remains a complex problem. Electric measurements cannot be taken directly from the bone without invasive surgery. Figure 4 illustrates the amount of fat, muscle, and other tissues surrounding the bone on a typical human thigh. In order to detect the change in conductivity and dielectric constant resulting from osteoporosis within a patient's bone, we must be able to take measurements non-invasively without the surrounding tissue interfering with the results.

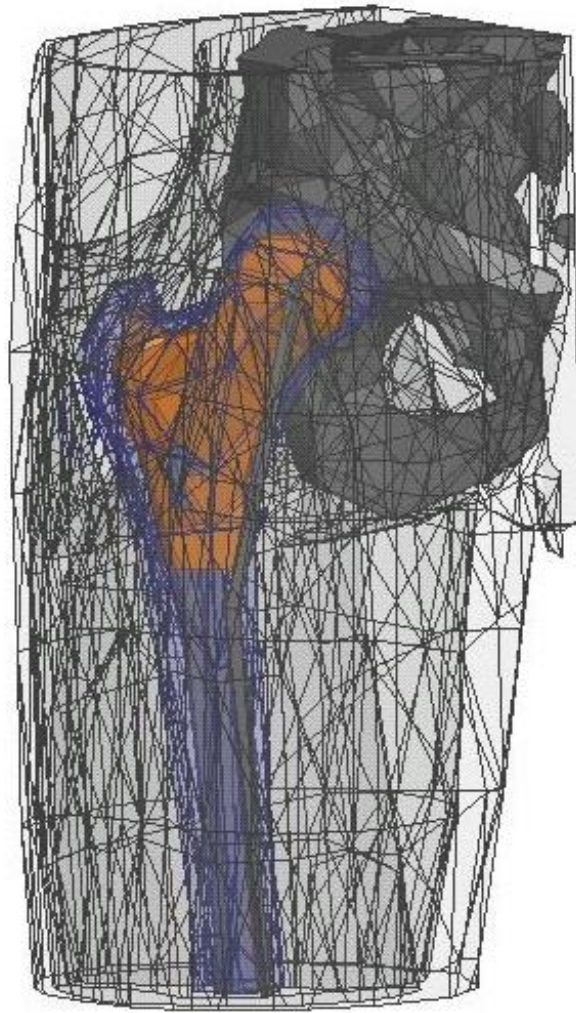


**Figure 5: Human Thigh Model [18]**

The following approaches to this problem explore several methods of injecting an electric signal into a human patient's extremity and extracting some measurable signal difference between bones of differing conductivity. With all of this information in mind, we can attempt to differentiate osteoporotic bone from healthy bone through electromagnetic measurements.

# Chapter 1 – Electrical Impedance Tomography

## I. Simulations Review

Before any physical measurements were performed, it was necessary to simulate the body's response to electrical current. Ansys Maxwell 3D, an electromagnetic design software was chosen as the platform for this analysis. The results of the simulations can be seen below:

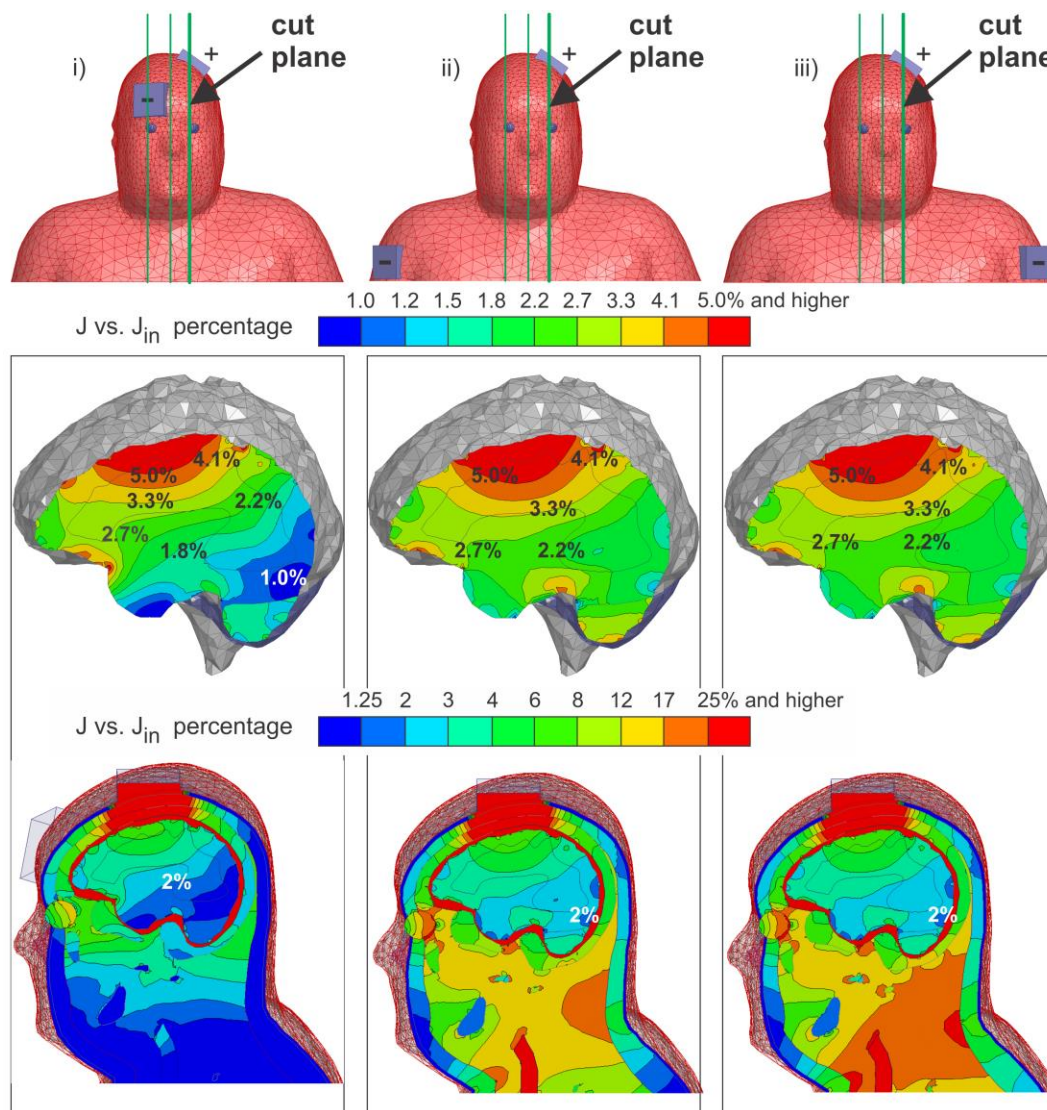


Figure 6: Central Cut Simulation Results [6]



Clearly, the maximum amount of current is concentrated directly underneath the positive and negative electrodes. It appears that the outside layer of the brain acts as a conductor, shielding the brain and allowing little current to penetrate deep into the gray matter. We can also see that for actual electrical impedance tomography, the best positions for the electrodes on the cranium would be the head and the shoulders, as this allows the most current to penetrate the brain, thus giving the most clear and concise results.

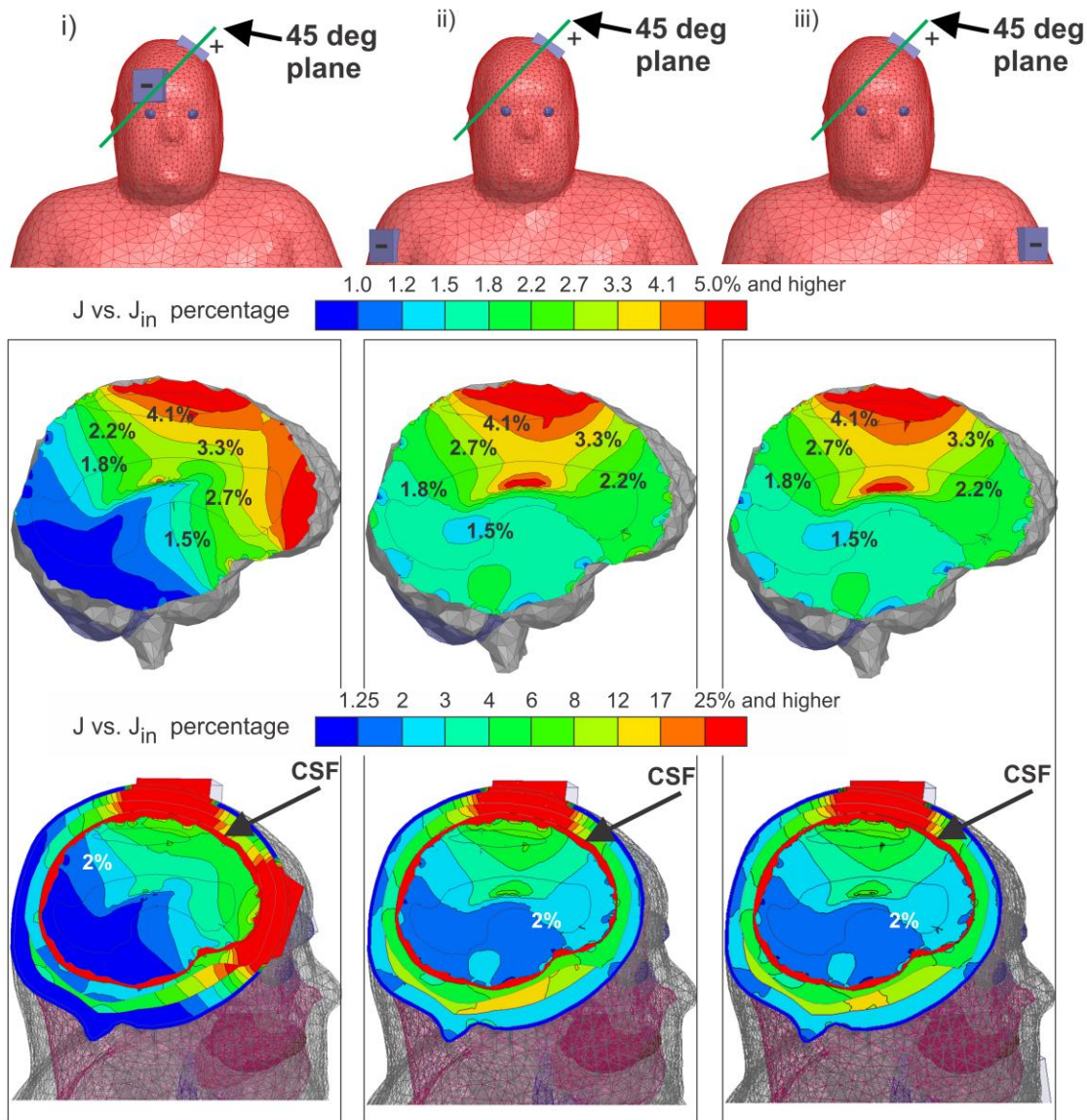


Figure 7: Forty-Five Degree Simulation Results [6]

With this in mind, simulations were performed with Ansys Maxwell 3D to determine the quality of the bone, a large frequency range to examine the differences between the bone with Osteoporosis and healthy bone. Figure 8 displays the percentage change in electrical property between a bone with the Osteoporosis and the healthy bone at different frequency ranges. The simulated result shows that as the frequency increases, the percent change decreases, which then stabilizes at about 6.6 percent.

The simulated result provides an acceptable indication that the healthy and osteoporotic bone presents several different electrical properties with changing frequencies. This difference is large enough for us to distinguish whether the bone is healthy or not. The aim was to obtain values above a six percent change in different parts of the bone. However, simulations resulted in inconsistent percent change between one and six percent. The figure below shows what a good result would look like compared to the simulation results.

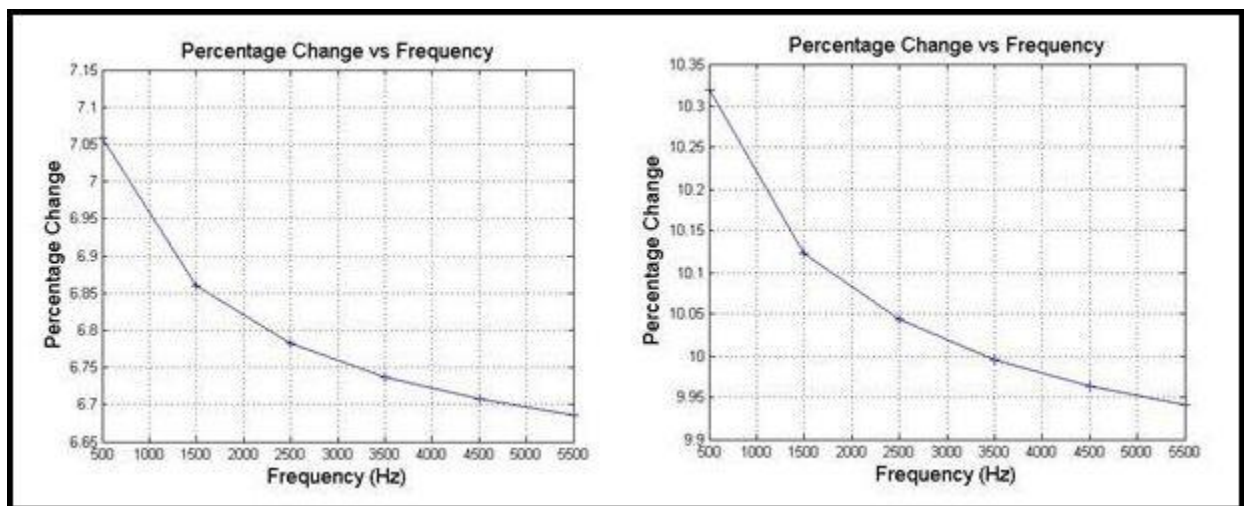


Figure 8: Electrical Property change in various Frequencies [2], [13]

## II. The Transconductance Amplifier

The first circuit we implemented was a voltage controlled current source which is represented by a transconductance amplifier. A small amount of electric current is injected into the body via the transconductance amplifier. When the body serves as the load, voltage measurements can be taken as the current flows through.

The circuit is made up of an Operational Amplifier (Op-Amp) with a power source for the supply inputs as well as an input voltage for the differential input of the op-amp and a reference resistor connected to ground. In ideal conditions, the OTA outputs a constant current given a differential input voltage value and a reference resistance value. This current is independent of the load resistance, which allows the freedom to connect the OTA to any given load and pump in a constant current. The LM348 was chosen for the op-amp as it is an industry workhorse and general all-purpose amplifier. The LM348 consists of four independent high-gain, internally compensated, low power amplifiers, all of which are designed to provide functional characteristics identical to those of the LM741.

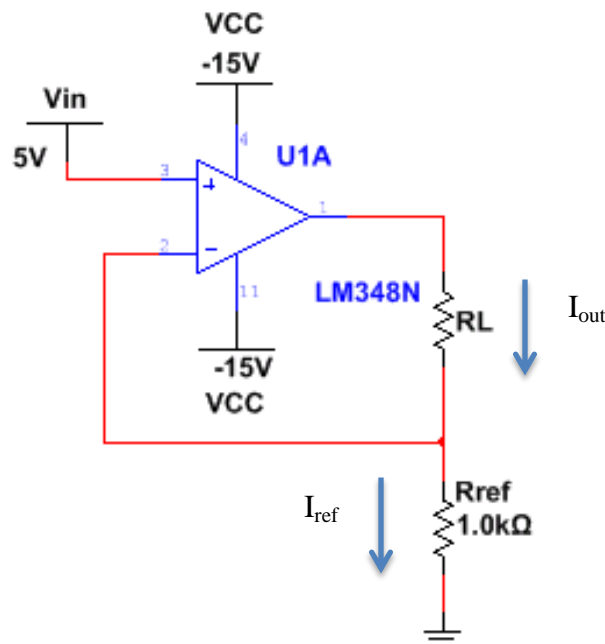


Figure 9: Operational Transconductance Amplifier Schematic

The transconductance of this circuit is defined as the change in output current over the change in input voltage:

$$g_m = \frac{\Delta I_{out}}{\Delta V_{in}} \quad (1)$$

The load current is defined as the differential voltage at the op-amp's inputs multiplied by the transconductance:

$$I_{out} = (V_{in+} - V_{in-}) \times g_m \text{ or } I_{out} = V_{in} \times g_m \quad (2)$$

Using Ohm's Law, the current through the reference resistor is determined by:

$$I_{ref} = \frac{V_{in+} - V_{in-}}{R_{ref}} = \frac{V_{in+} - 0V}{R_{ref}} = \frac{V_{in+}}{R_{ref}} \quad (3)$$

Since there is 0V at the  $V_{in-}$  input, the same current flows through both  $R_{ref}$  and  $R_L$ :

$$I_{ref} = I_L = \frac{V_{in+}}{R_{ref}} \quad (4)$$

From here, we can easily solve for the transconductance of our OTA:

$$\frac{I_L}{V_{in+}} = \frac{1}{R_{ref}} \quad \frac{\Delta I_{out}}{\Delta V_{in}} = \frac{1}{R_{ref}} \quad g_m = \frac{1}{R_{ref}} \quad (5)$$



As you can see, the transconductance of the OTA circuit is determined by the value of the reference resistor,  $R_{\text{ref}}$ . Furthermore, the output current,  $I_L$ , is independent of the load resistance  $R_L$ . The input voltage  $V_{\text{in}+}$  and the reference resistor  $R_{\text{ref}}$  determine the current output by the OTA. This makes the OTA an attractive choice for applications that require a certain current for any number of different load impedances.

### III. Printed Circuit Board (PCB) Fabrication

In order to assure a steady supply of current with fewer wires and components we decided to outline, design, and produce a printed circuit board. A combination of two common circuit and board design programs, *Multisim* and *Ultiboard*, were used to design the PCB. The original circuit consisted of an LM348N Operational Amplifier, a single control resistor, and six outputs, making it a relatively simple circuit to produce. The *Multisim* simulation circuit below in figure 10:

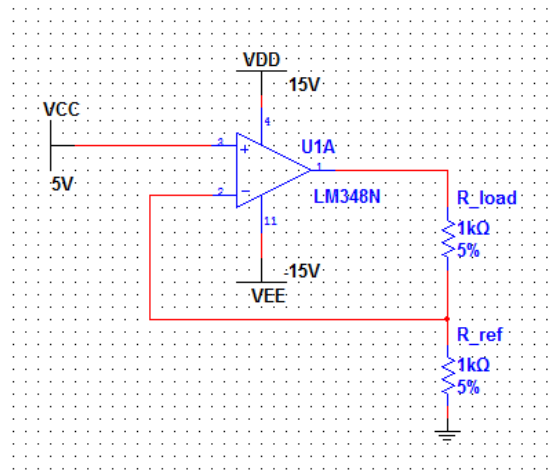


Figure 10: Multisim Simulation Circuit

In order to produce the circuit board one must have an outline of the circuit with all of the components laid out as they will be built. *Ultiboard* was the program chosen for the circuit board layout due to our team's familiarity with it. The *Ultiboard* outline was used to produce the PCB using the toner-acid backmasking process. The *Ultiboard* outline is shown below:

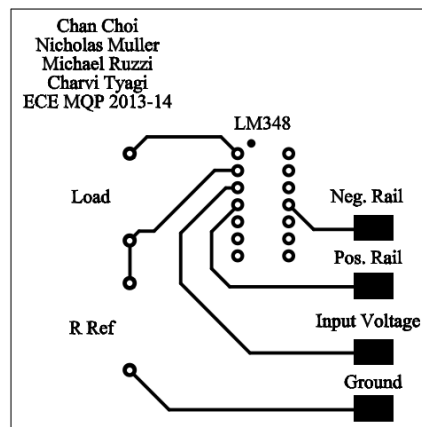


Figure 11: Ultiboard Design Output

### III-i. Toner-Acid Backmasking Process

The toner-acid backmasking process is a method to produce a PCB in a relatively short amount of time. Most of the time fabricating a PCB is generally taken up in the design process, so the production proceeds fairly quickly once that is complete. First the *Ultiboard* design is printed onto a piece of glossy paper mirrored, and then reversed using a high-density LaserJet printer. This is then placed toner side down onto a blank PCB board, and then heat is applied to the paper via a common household iron. What this does is transfer the toner from the glossy paper to the blank PCB, the image is now right side up and flipped back to the normal orientation on the PCB.

The PCB is then submerged into a combination of one part Muriatic Acid and two parts Hydrogen Peroxide; this dissolves the copper from the PCB on every area except the area that is protected by the toner. Once all the components are mounted and soldered, you have a finished product as seen below:

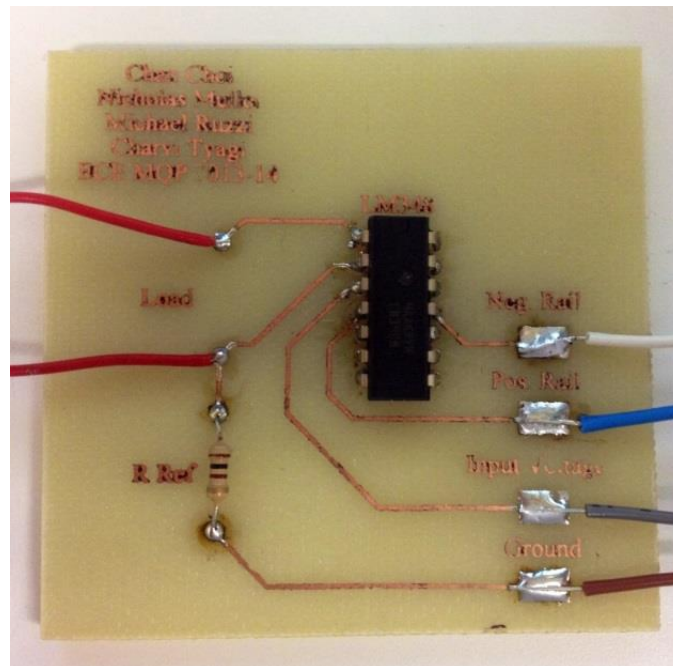


Figure 12: Finished PCB for OTA Circuit

## IV. Device and Materials

### IV-i. Basic Medical Phantom

In order to test the theory of this MQP, a phantom was constructed that replicates the electrical characteristics of the human arm. This was accomplished using a clear Plexiglas tube of two and one quarter inches in diameter studded with a series of electrodes and a central nylon rod. The electrodes have to be in contact with the conductive medium, which meant that holes had to be drilled through the non-conductive PVC and the electrodes were permanently mounted inside. As they are permanently mounted, a total of five pairs of electrodes were used to fully explore all the possible combinations of electrode spacing and positioning. One pair was positioned in opposition to each other, a second pair in opposition was placed above and rotated ninety degrees, another pair was placed directly above and below each other, the fourth and fifth pair were placed in opposition ninety degrees apart.



Figure 13: Basic Phantom Device

#### IV-ii. Modeling Human Body Tissues

The actual tissue was replicated using a simulant liquid that mimics the dielectric characteristics of human tissue; this material was based on a mixture of De-ionized water, Triton X-100, and Diethylene Glycol Butyl Ether (DGBE) as pioneered by Gimm [19].

The simulant liquid is a fifty-fifty blend of de-ionized water and auxiliary liquid plus one percent salt by weight. The auxiliary liquid itself is two thirds Triton X-100 and one third DGBE. This combination yields a stable, viscous, and conductive liquid that retains the correct permittivity from DC to 830 MHz.

Ingredient	Percentage
De-Ionized Water	49.00%
Triton X-100	33.33%
DGBE	16.67%
Salt (NaCl)	1.00%

**Table 1: Simulant Liquid [19]**

#### IV-iii. Conductive Plastics

One possibility that was also explored was the potential use of solid conductive plastics that would reproduce the semi-conductive properties of human skin. A number of potential materials were identified using CES Edupack, a standard material properties database. After narrowing down the selection to polymers and materials with a fairly high resistivity, only a few families of materials were left. After further deliberation carbon-doped plastics were chosen as they had the best electrical properties while also being fairly inexpensive.

Several members of the MQP group then visited a number of polymer manufacturers around the Worcester, MA area that carried carbon-doped plastics. Unfortunately, it was found that the plastics that were chosen did not have the electrical properties that were sought after.

It seems that manufacturing tolerances vary considerably among manufacturers and electrical resistance is not standardized. After testing a half-dozen samples it was decided that conductive plastics would not be pursued and the electrodes would be permanently mounted to the medical phantom.

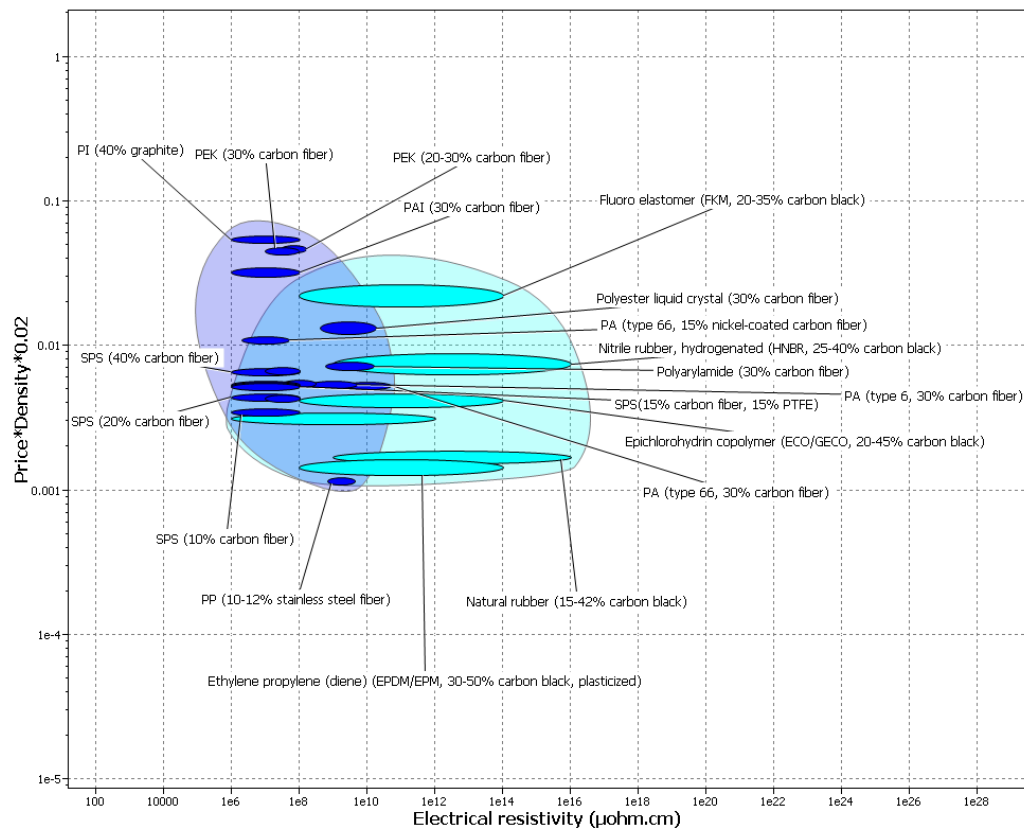


**Figure 14: Potential Semi-Conductive Materials**

## **V. Electrical Impedance Tomography**

A variety of medical problems requires knowledge of the time-varying distribution of electrical properties inside the body. "Electrical properties" define the electric conductivity and permittivity. The electric conductivity is a measure of the ease with which a material conducts electricity and the electric permittivity is a measure of how the charges within a material separate under when an electric field is applied. If the material has high conductivity, it will allow both direct and alternating currents to pass through. On the other hand, high-permittivity materials only allow the passing of alternating currents. The study of these properties is of high interest in medical applications because different tissues have different conductivities and permittivities.

Electrical impedance tomography (EIT) is a relatively new imaging method that has been rising rapidly over the past twenty years. It holds great potential in clinical diagnosis. EIT is a process in which a system uses electrical measurements to reconstruct and display approximate pictures of the electric conductivity and permittivity inside the body. This is usually achieved by designing an electronic system that applies small alternating currents through electrodes attached to the surface of the body and measures the resulting voltage. The term "impedance" is the ratio of the voltage across a circuit element to its current [3]. The key goal of EIT is to produce images that are physiologically useful. EIT is capable of creating two types of image. The first is known as difference imaging, where a change in ratio or percentage represents some physiological parameter like blood volume or cell size. The second is known as absolute imaging, which produces an image of the absolute conductivity or permittivities. This absolute method of imaging is more difficult than the difference method, since the contact impedance of the electrodes cannot be accurately described when making clinical measurements [1].

A vital question often raised about new imaging methods is their role in the clinical domain. EIT has the potential of playing a crucial role in diagnostics and monitoring of various disease conditions, which range from detection of breast cancer to monitoring brain function and possibly stroke.

However, EIT is not a common tool used in everyday clinical practice yet. What the medical industry is looking for is a method that does not use ionizing radiation and is safe and cheap. At present, the key advantage of EIT is its temporal resolution—it does not have the spatial resolution of other methods like MRI or computer tomography.

The basic physical properties of the human tissues should also be taken into consideration. When a body performs different kind of activities, the bioimpedance of the body produces a lot of information about the changes of the body. For example, the measured impedance is dependent on the amount of water in the body. The measurement of bioimpedance includes the characterization and identification of cells based on their impedance. This is based on their size, orientation, and membrane thickness and can vary from cell to cell [1]. In EIT this impedance information is used to form images of the insides of the human body.

Another important aspect to study is the electric properties of biological tissues. Tissue consists of thin cells and membranes that have high resistivity and can behave as small capacitors. Two important properties of the impedance of biological tissues are the resistance and reactance. The resistive component comes from the conductive characteristics of bodily fluids while the cell membranes create a frequency-dependence. EIT comes into play by imaging these impedance properties. The impedance measurements of biological tissue can be made as low as 20 Hz up to 1 MHz frequencies [1]. When measuring using high frequencies, the current passes right through these capacitors. At low frequencies, however, the membranes impede current flow. Bioimpedance can therefore be used to measure volumes, shapes, or tissue electrical properties. The mathematical model for EIT is described below from Dr. Margaret Cheney's article about "Electrical Impedance Tomography" [3]:

The electric potential  $u$  in the body  $Q$  is governed by the equation

$$\nabla \cdot \gamma(x, \omega) \nabla u = 0 \quad (6)$$

Here  $x$  is a point in  $\Omega$ ,  $u$  is the electric potential or voltage, and the admittivity  $\gamma$  is given by  $\gamma(x, \omega) = \sigma(x, \omega) + i\omega\epsilon(x, \omega)$ , where  $\sigma$  is the electric conductivity,  $\epsilon$  is the electric permittivity, and  $\omega$  is the angular frequency of the applied current. It is the admittivity of a block of homogeneous material that is proportional to the reciprocal of its impedance.



In practice, we apply currents to electrodes on the surface  $\partial\Omega$  of the body. These currents produce a current density on the surface whose inward pointing normal component is denoted by  $j$ . Thus,

$$\gamma \frac{\partial u}{\partial \nu} = j \text{ on } \partial\Omega \quad (7)$$

One possible model for EIT is (6) and (7) together with the conservation of charge condition  $\int_{\partial\Omega} j = 0$  and the condition  $\int_{\partial\Omega} u = 0$ , which amounts to choosing a "ground" or reference voltage. This model is the commonly used *continuum model*. For the continuum model, we define the operator  $R$  by  $Rj = v$ , where  $v$  denotes the restriction of  $u$  to the boundary. Unfortunately, the continuum model is a poor model for real experiments, because we do not know the current density  $j$ . In practice, we know only the currents that are sent down wires attached to discrete electrodes, which in turn are attached to the body. One might approximate the unknown current density as a constant over each electrode (the gap model), but this model also turns out to be inadequate. We need to account for two main effects: the discreteness of the electrodes, and the extra conductive material (the electrodes themselves) we have added. We can do this as follows. The integral of the current density over the electrode is equal to the total current that flows to that electrode. Thus we have;

$$\int_{e_l} \gamma \frac{\partial u}{\partial \nu} ds = I_l \quad l = 1, 2, \dots, L \quad (8)$$

Where  $I_l$  is the current sent to the  $i^{\text{th}}$  electrode and  $e_l$  denotes the part of  $\partial\Omega$  that corresponds to the  $i^{\text{th}}$  electrode. This is combined with

$$\gamma \frac{\partial u}{\partial \nu} = 0 \quad \text{in the gaps between electrodes.} \quad (9)$$

The conventional way to model the very high conductivity of the electrodes is to enforce the constraint that  $u$  is constant on each one. These constants, which we denote by  $V_l$ , are the voltages we measure. We write these constraints as

$$u = "V_l" \text{ on } e_l, \quad l = 1, 2, \dots, L \quad (10)$$

Where the quotes are used to remind us that the  $V_l$  are not specified in advance but are part of the solution of the forward problem.

This model we call the *shunt model*. The shunt model, unfortunately, doesn't give results that agree with experimental data either. It fails to account for an electrochemical effect that takes place at the contact between the electrode and the body. This effect is the formation of a thin, highly resistive layer between the electrode and the body. The impedance of this layer is characterized by a number  $z_l$ , which we call the effective contact impedance or surface impedance. We therefore replace constraint (10) by

$$u + z_l \gamma \frac{\partial u}{\partial \nu} = "V_l" \text{ on } e_l \quad l = 1, 2, 3, \dots, L \quad (11)$$

The resulting model we call the complete model. The complete model consists of (6), (7), (8), (9), and (11), together with the conditions

$$\sum_{l=1}^L I_l = 0 \quad (\text{conservation of charge}) \quad (12)$$

and

$$\sum_{l=1}^L V_l = 0 \quad (\text{choice of a ground}) \quad (13)$$

This model has been shown to have a unique solution. It is able to predict the experimental measurements to better than 0.1% [1]. Before EIT can prove to be a clinically useful device, many challenges remain that need to be overcome. The challenges can be classified into the areas of electronics, algorithms, and clinical applications. This is not to say that it does not have the capability to produce useful clinical results. Another important consideration is the development of reconstruction algorithms, and until the best available algorithms are used with all available prior information, clinically useful data will not be achievable from EIT. However, EIT still has great potential and its contribution to these areas should not be underestimated. The variations that are appearing could hold the key to the future development of EIT. A combination of the advantages of EIT and other imaging methods may prove to be of great clinical value.

## VI. Howland Circuit

The Basic Howland current pump [12], [16] is another circuit that can be used for either a current source or current sink in various applications. The Howland current pump is excellent for testing other devices as it can be used to force specific currents into sensors or other materials. The circuit itself is also useful in production tests, or setting test conditions for experiments. This circuit is comprised of an op-amp with a power source for the supply inputs as well as an input voltage for the differential input of the op-amp, and four resistors R1-R4. The feedback from the output through both the positive and negative feedback loops is at equal strength, so the ratios of R1/R3 and R2/R4 are the same. The schematic for the Howland current pump circuit can be seen in the figure below.

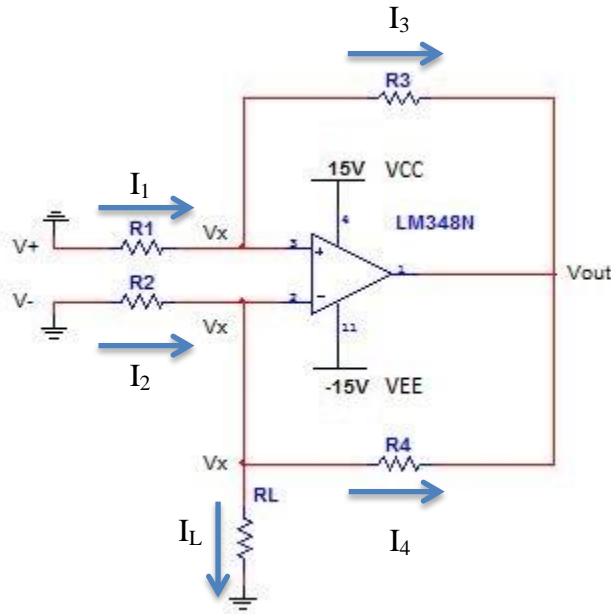


Figure 15: Howland Current Pump Circuit

The derivation of this circuit is fairly straightforward. We can start by observing Kirchhoff's Current Law at each of the nodes labeled  $V_x$ .

$$I_1 = I_3 \quad (14)$$

$$I_2 = I_4 + I_L \quad (15)$$

Next, we take the above two equations and express them in terms of voltage and resistance.

$$\frac{V_+ - V_X}{R_1} = \frac{V_X - V_{out}}{R_3} \quad (16)$$

$$\frac{V_- - V_X}{R_2} = \frac{V_X - V_{out}}{R_4} + I_L \quad (17)$$

Since the ratios of the resistors  $R_1/R_3$  and  $R_2/R_4$  are the same we can rewrite equation (16):

$$\frac{V_+ - V_X}{R_2} = \frac{V_X - V_{out}}{R_4} \quad (18)$$

Now we substitute  $\frac{V_+ - V_X}{R_2}$  back into equation (17):

$$\frac{V_- - V_X}{R_2} = \frac{V_+ - V_X}{R_2} + I_L \quad (19)$$

Finally, we solve for  $I_L$ :

$$I_L = \frac{V_- - V_X}{R_2} - \frac{V_+ - V_X}{R_2} \quad (20)$$

$$I_L = \frac{V_- - V_+}{R_2} \quad (21)$$

Inversely, if we were to connect the load to the positive feedback loop, instead of the negative feedback loop, and solve for  $I_L$  the same way, we would find:

$$I_L = \frac{V_+ - V_-}{R_2} \quad (22)$$

When the load is connected to the positive feedback loop the gain is found to be the output over the input. For the Howland current pump, this is the output current  $I_L$  over the input differential voltage ( $V_+ - V_-$ ):

$$\frac{I_L}{V_+ - V_-} = \frac{1}{R_2} \quad (23)$$

$$\frac{\text{output}}{\text{input}} = \frac{1}{R_2} \quad (24)$$

$$G = \frac{1}{R_2} \quad (25)$$

When the load is connected to the negative feedback loop, and the gain is solved for the same way, it is found to be negative:

$$G = -\frac{1}{R_2} \quad (26)$$

As we can see in the derivation above, the Howland current pump is composed of a positive and a negative feedback loop. The output current is dependent upon the input voltage and the value of the resistor connected before the op-amp's input in the feedback loop connected to the load. In this manner, the Howland current pump can serve as either a current source or a current sink based on which feedback loop the load is connected to. Once again, the output current is independent of the load, making the Howland current pump a useful circuit for many applications where a constant input current is required for a variety of different load impedances. One notable downside of the Howland circuit is that four resistors must be near perfectly matched or the functionality of the circuit might be compromised. In order for this to be achieved, precision resistors on the order of 0.01% error are required and these resistors don't come cheap!

If we consider the entire Howland circuit a black box with both differential inputs grounded, then we can connect a voltage source with a series resistor to the load in order to determine the output impedance. In this manner, we can input a voltage through a resistor, and calculate the current input into the black-box using Ohm's law.

$$I_{in} = \frac{V}{R_{series}} \quad (27)$$

Multiplying the input current with the value of the series resistor gives the voltage across the series resistor:

$$V_{series} = I_{in} * R_{series} \quad (28)$$

The voltage input to the black box can be determined by subtracting the voltage across the series resistor from the total voltage input:

$$V_{in} = V - V_{series} \quad (29)$$

Substituting equation (28) into (29), we find:

$$V_{in} = V - ( I_{in} * R_{series} ) \quad (30)$$

With the voltage and current input into the Howland circuit black box, we can solve for the output impedance:

$$Z_{in} = \frac{V - ( I_{in} * R_{series} )}{I_{in}} \quad (31)$$

Dividing the voltage input into the black box by the current input into the black box solves for the output impedance.

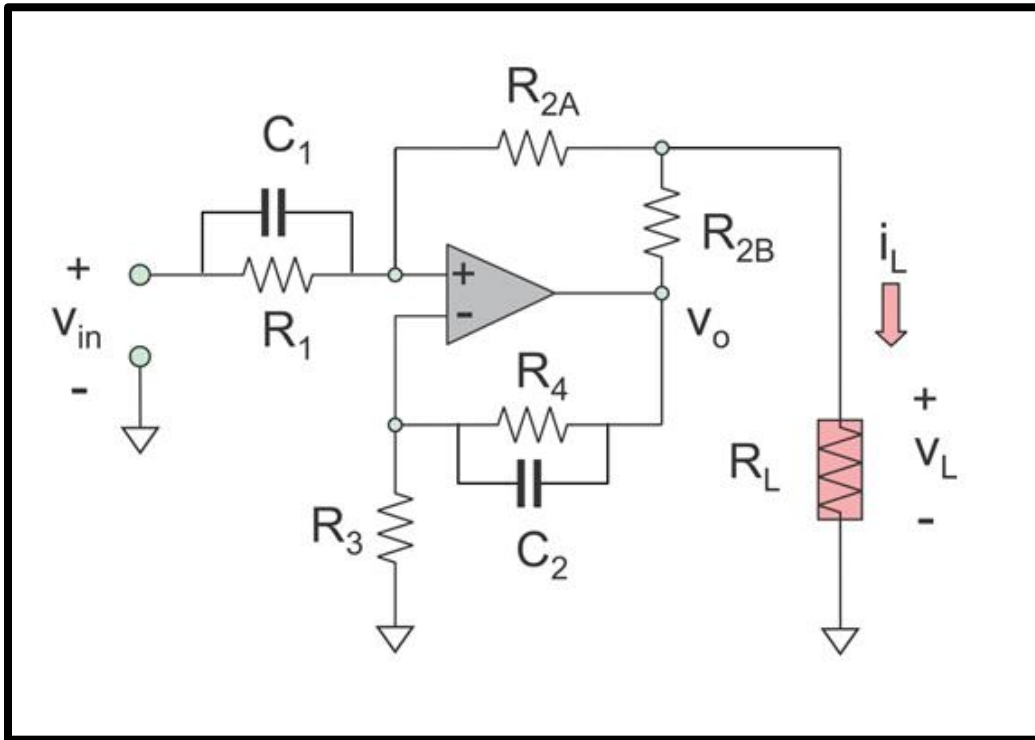


Figure 16: Advanced Howland Circuit [12], [16]

## VII. Results

In our first approach, the medical phantom was filled with a mixed solution meant to model the conductivity and dielectric constant of healthy bone tissue. The transconductance amplifier was then used to inject a small amount of current directly into the solution at different electrode inputs. Next, a rod of material with little to no conductivity was inserted into the solution. This rod was made to model an osteoporotic patient by lowering the overall conductivity of the solution. An oscilloscope was hooked up to the tube setup at separate input and used to measure the voltage change across the solution after the osteoporotic model was inserted. Figure 16 displays the setup used for this experiment.

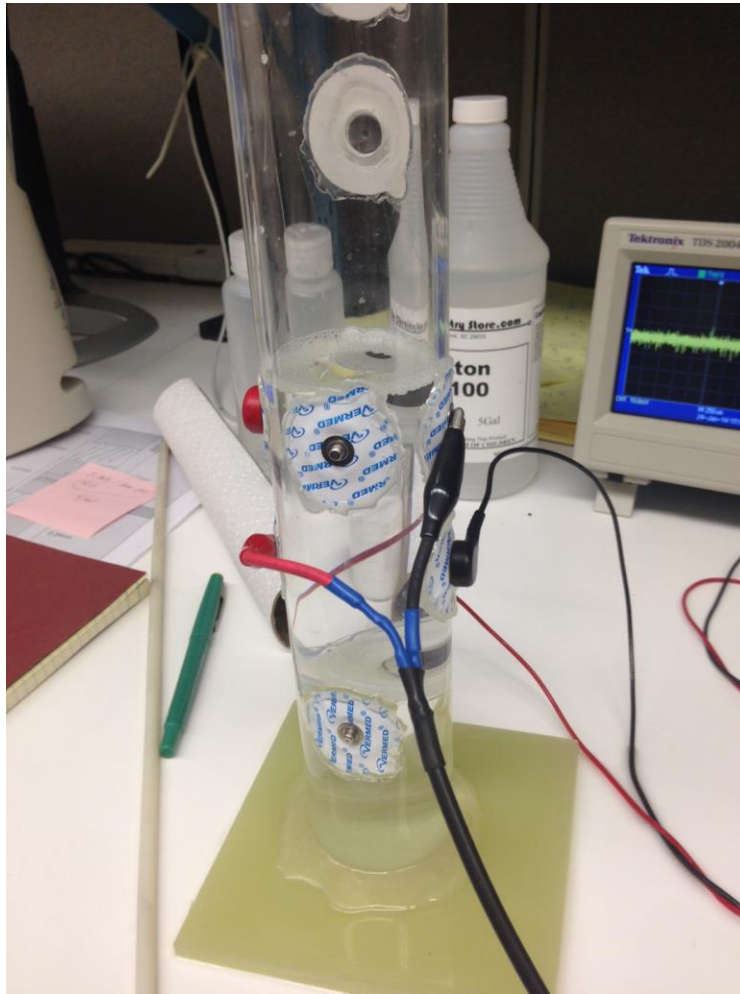


Figure 17: Experimental Impedance Tomography Setup

Our results for the impedance tomography setup were inconclusive. We did not measure consistent voltage changes across different electrode positions. The sensitivity of the setup was very low, and an unusual voltage drift of about  $\pm 400\text{mV}$  was observed. We can account for these sources of error in a few ways. First, a more accurate model of an osteoporotic patient could have been achieved through the removal of the displaced solution when the rod is inserted into the setup. Additionally, the drifting voltage response may have been due to the background RF of the various electronics in our lab that we were not able to shield against.

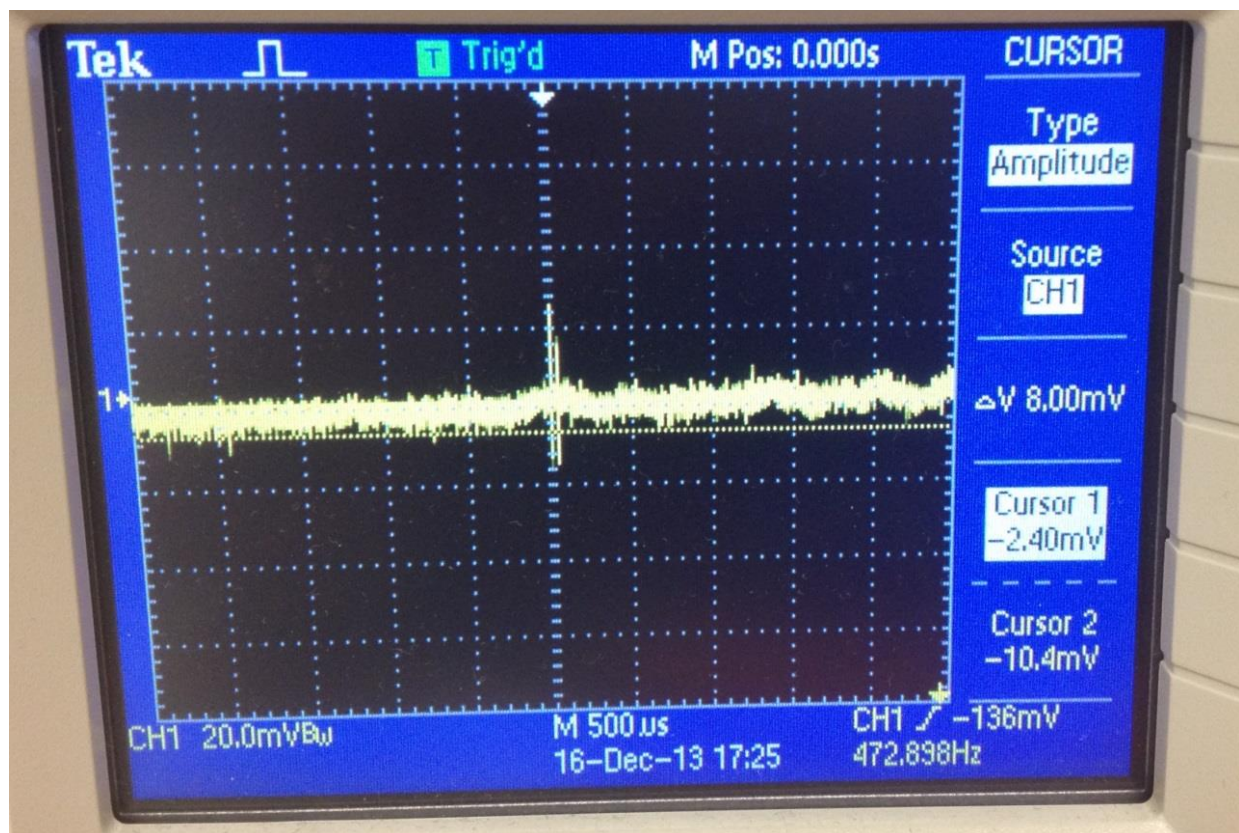


Figure 18: DC Current Injection Oscilloscope Results

Figure 17 shows the most definitive voltage measurement for our DC current injection experiment. The major disadvantage of this experimental setup was the difficulty involved in injecting current into our liquid bone model.



The current would not easily and reliably flow through the solution and provide consistent voltage measurements. Therefore, the DC current injection method would not be ideal for measuring changes in the bone's electrical qualities. Our next approaches to this problem involve injecting a signal that can pass more easily through our bone model and hopefully provide more consistent measurements. In the proceeding experiment, we will look to inject an infrared signal into the body and measure the signal change without interference due to current drift or current flow issues.

## **Chapter 2 – Near Infrared Scattering Sensors**

### **I. Background**

Several applications of infrared spectroscopy have been developed in the last decades to examine and to better understand the human body. Technological development in the medical industry has created various minimally invasive techniques for examining functional brain activity. Examples of such techniques include Electroencephalography (EEG), Positron Emission Tomography (PET), Magnetoencephalography (MEG), and the latest functional Magnetic Resonance Imaging (fMRI). Brain activity is associated with changes in the optical properties of the subjects' brain tissue. These optical measurements can assess different properties of the brain during its activation.

Currently, it is possible to access the brain and study brain activity in human subjects non-invasively using near-infrared light—light that can enter biological tissue and allow the study of the brain activity. This lesser-known technology for monitoring brain function focuses on the absorption and scattering properties of near-infrared light, which is useful to study brain activity [15]. These near-infrared imaging devices are being used for low-resolution functional brain imaging. Advantages of the optical methods include “biochemical specificity, temporal resolution in the millisecond range, the potential of measuring intracellular and intravascular events simultaneously, and the portability of the devices” [17]. The most important advantages compared to other methods are the portability, unobtrusiveness, low power, and low cost. Also in comparison, these optical methods can provide great temporal and spatial sensitivity. The qualities of the optical approach are primarily overlooked and it is crucial to understand the great possibilities that this technology can produce.

For example, the fact that this method is noninvasive, and with proper fiber coupling, there will be a higher tolerance for movement; which will allow the study of infants, small children, and other patients with movement disorders [15]. The portability of a potential device allows bedside monitoring, so patients can be monitored for extensive periods of time, this can also be useful for studying the effects of slow-acting drugs.

Moreover, the near infrared light method is non-ionizing, which means patients and doctors do not have to be concerned about the number of scans the patient can undergo. However, with advantages always come limitations. These optical methods cannot provide very precise anatomical localization with respect to the brain, and this method also has poor depth penetration and localization.

NIR-spectroscopy and imaging is still in the early phase for applications in the neurosciences. Accurate determinations are still difficult without implementation of more sophisticated approaches. Therefore, there is not much current studies can report. It is known however, that the NIR approach definitely holds its advantages in contrast to other techniques. The greatest attraction to NIR imaging systems is that the cost of even highly sophisticated imaging systems of the future will be much less than those of other neuroimaging devices.

Another common application of infrared spectroscopy is measuring the level of oxygenation inside the body. To treat a critically ill patient, detecting and delivering the appropriate amount of oxygen that the tissue demands is the key to a fast recovery. Pulmonary arterial catheterization is a highly invasive technique that determines the patient's oxygen delivery and oxygen extraction capabilities [5]. But this technique requires an intensive procedure, which is time consuming and very expensive.

Using infrared technology such as a tissue spectrometer, which is a noninvasive technology that quantitatively measures the oxygen saturation directly in muscle tissue using near infrared light, one can produce a result without having the patient undergo an invasive surgery [4]. The use of infrared spectroscopy has not only made the process cheaper but since it does not require many corresponding devices to follow, it has made the device portable as well. Even in the field of anesthesiology, the use of infrared spectroscopy is becoming popular. Managing the proper oxygen level in the brain is the key to a successful anesthesia procedure. Infrared spectroscopy is used as cerebral oximetry monitoring device to detect any brain ischemia. One of the most common limitations has been the absence of a set procedure based on physiology when treating decreases in regional cerebral tissue oxygen saturation.

Near Infrared Spectroscopy (NIRS) is also widely used to evaluate food for animals, and humans as well, to examine the nutritional value of the food. Evaluating the nutritional facts of the food, whether the animal is taking right amount of nutrients could determine the healthiness of the animal, which could possibly prevent diseases as well as possibly preventing any environmental issues [11]. Good evaluation of nutrients could allow farmers to save money on feed cost. NIRS is specifically suited for this purpose because NIRS gives more precise measures, and unlike other chemical methods that have been previously used, which takes days to gather the result, NIRS can gather results within seconds after the measurements were taken.

The technology for the use of infrared lights has existed since the 1800s, but since the demand for a low cost, rapid technique for in depth precision measurements has risen, NIRS became the most popular method to do the job. NIRS does have limitations, such as having different optical value from device to device, causing data transfer error. Another disadvantage is that it needs a highly precise spectroscopic instrument to function. But even with these drawbacks, NIRS is a well recommended method over other measurement techniques.

## II. Simulations and Results

The last method applied to study the bone characteristics was the infrared scattering sensors approach. In this part, the aim was to understand how the application of scattered light through a part of the body would affect the resulting infrared signal. As discussed, this noninvasive approach is preferred and especially of interest because of its low cost and the elimination of any harmful side effects due to the fact that near infrared light is non ionizing. Doctors and patients do not have to be concerned about the number of scans since the patients could undergo multiple scans as needed without too much risk.

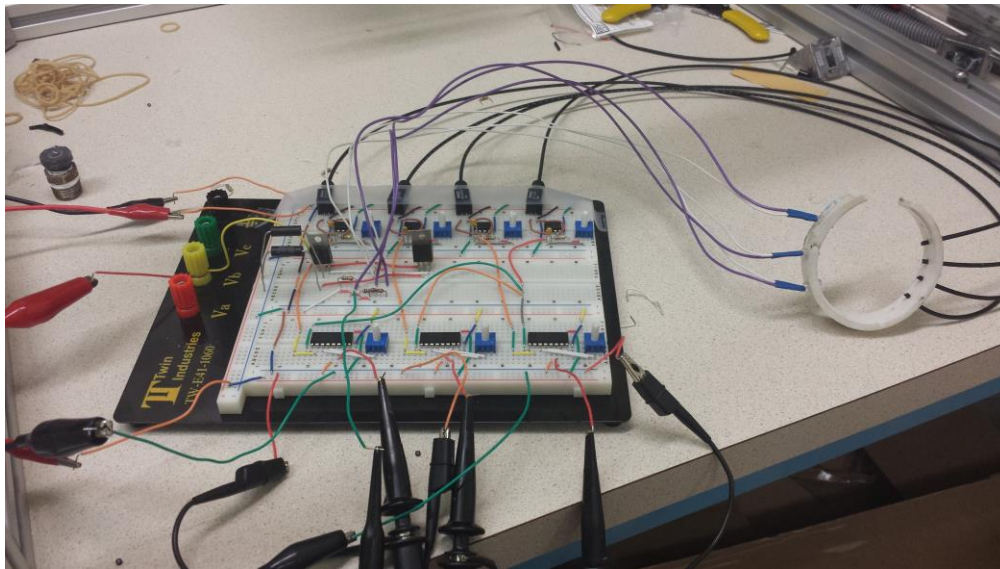
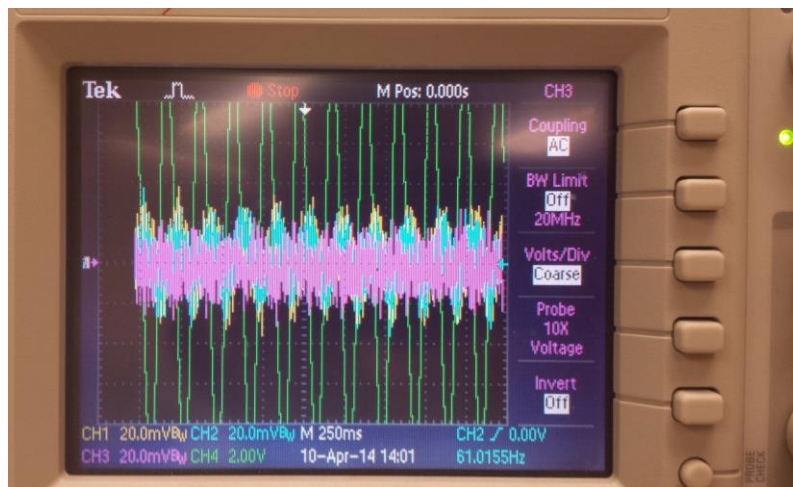


Figure 19: Infrared scattered sensors setup

The experiment setup is shown in Figure 16. A wrist band shown on the right side was hooked up to a circuit board. The first stage of the circuit was comprised of four trans-resistance amplifiers that provided the current source for the LEDs. In the second stage, we have three instrumentation amplifiers as the inputs to the circuit. The wrist band has three infrared LEDs along the left side that can transmit an infrared signal across the band to the receiver on the other end. In the first case, there was copper foil wrapped around the wrist band covering the LEDs, as shown in Figure 17.



**Figure 20: Wrist band covered with copper foil**



**Figure 21: Waveform for band covered with foil**

Since the IR signal is being blocked by the copper foil, the receiver is not able to detect any signals. Therefore, in the resulting signals in Figure 18, a fair amount of noise is observed. However, in the second case the copper foil was removed and wrist band was attached to a wrist. In this scenario, the IR signal traveled through the wrist and was detected by the receiver on the other side of the band. As a result, a slight change in the waveform is visible in Figure 20. The pink and blue channels experience an amplification once the wrist is inserted into the band.

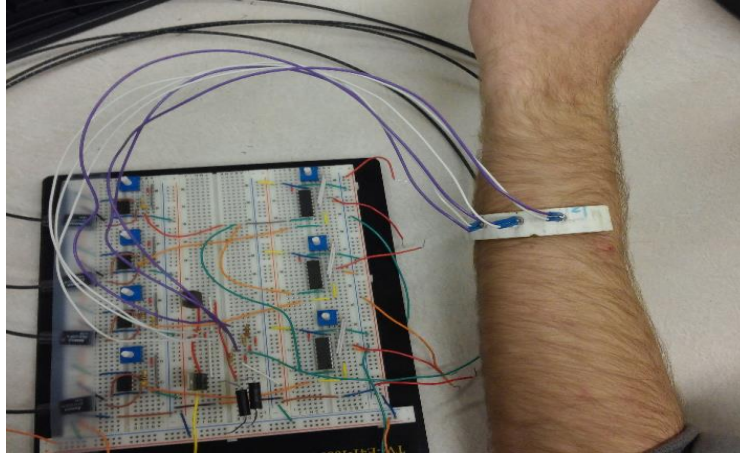


**Figure 22: Set up of wrist band on the wrist**

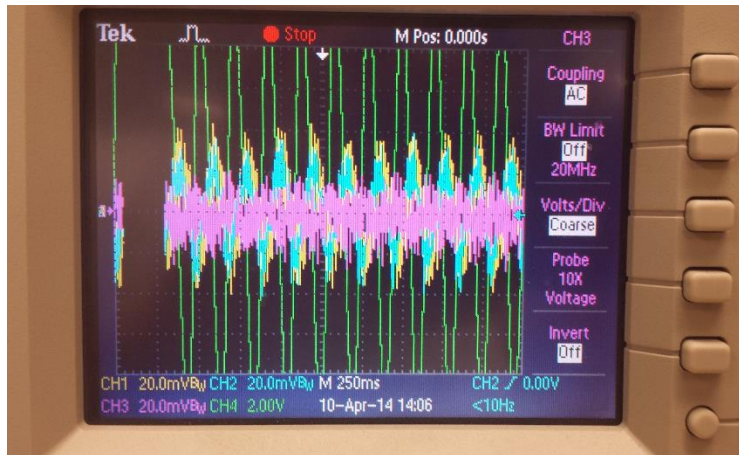


**Figure 23: Waveform of IR signal across wrist**

The change in waveform between the two cases, though slight, proved to be a satisfactory result as of now because the change accounts for the infrared signal being detected through the wrist by the receiver. This method can be used in further studies of different bone samples with osteoporosis or any other bone disease by observing how the signals are altered when a part of the body is inserted into a band. The band in this specific experiment is only practical for the wrist or maybe ankle because the infrared signal can only penetrate about 2.5 cm. The thigh, for example, would not work as there is large amount of muscle and fat that the signal would have to pass through and would not be able to reach the bone. This matter can be worked upon in the future, to increase the depth of the signal so other parts of the body can also be studied.

## Chapter 3 – Microwave Antenna Sensors

### I. Background

The third approach we used to detect the electrical differences between osteoporotic bone and healthy bone is the use of dual loop antennas. Loop antennas are typically either small loop or resonant loop type antennas. Their applications range from radio frequency receivers or transmitters, to high frequency broadcast and radio amateur applications, to VHF and UHF communication systems such as satellite radio or government/military transmissions. Our near field antenna system is connected to a set of unbalanced transmission lines corrected by a balanced-to-unbalanced device, or balun, and measures the amount of power transferred from one antenna to the other through the conductive medium inside the Plexiglas tube setup. This difference in transmitted power correlates to the transmission coefficient.

When we alter the conductivity of the solution inside the tube setup by introducing a tube of air—which models osteoporotic bone by lowering the overall conductivity of the tube’s contents—we can measure the change in transmission coefficient with a network analyzer. This change of transmission coefficient is represented on the network analyzer by a shift in the signal’s resonances. Therefore we can establish that if we build a dual loop antenna setup that consistently measures a significant resonance shift when the conductive medium is changed from the osteoporotic model to the healthy model, then this antenna setup could be used to measure electric differences in actual bone samples. And if our dual loop antenna system can measure the transmission coefficient shift in actual bone samples, then our method of differentiating healthy bone from osteoporotic bone can be studied and used to detect osteoporosis or other bone disease.



## II. Antenna Simulations

This project used Ansys HFSS Maxell, an electromagnetic finite element method solver; to calculate the antenna transmission parameters of our prospective antennas. Ansys was used by Mr. Janakinadh Yanamadala to create the antenna model that we implemented. Mr. Yanamadala noticed that when two loop antennas were placed around a human limb and one antenna was angled at thirty degrees, a noticeable shift in the antenna transmission coefficients occurred.

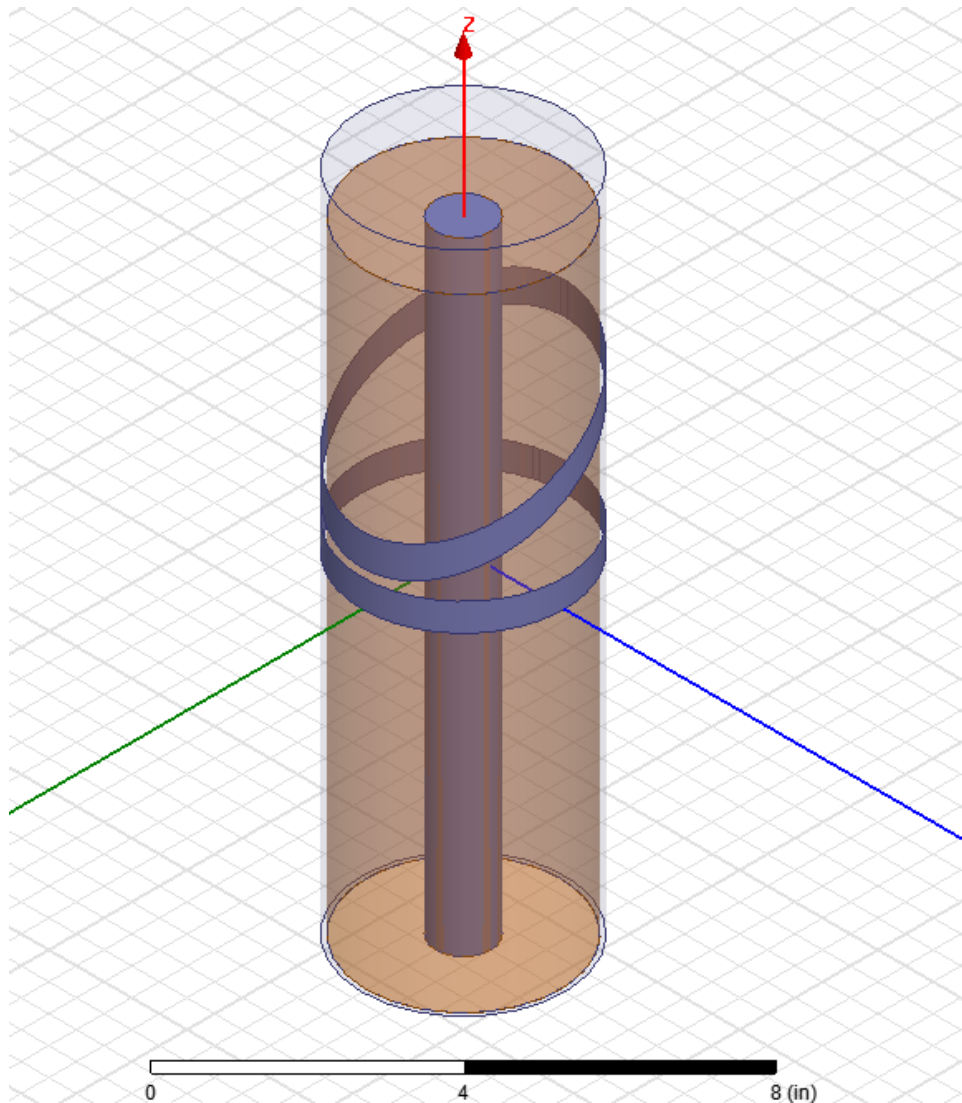
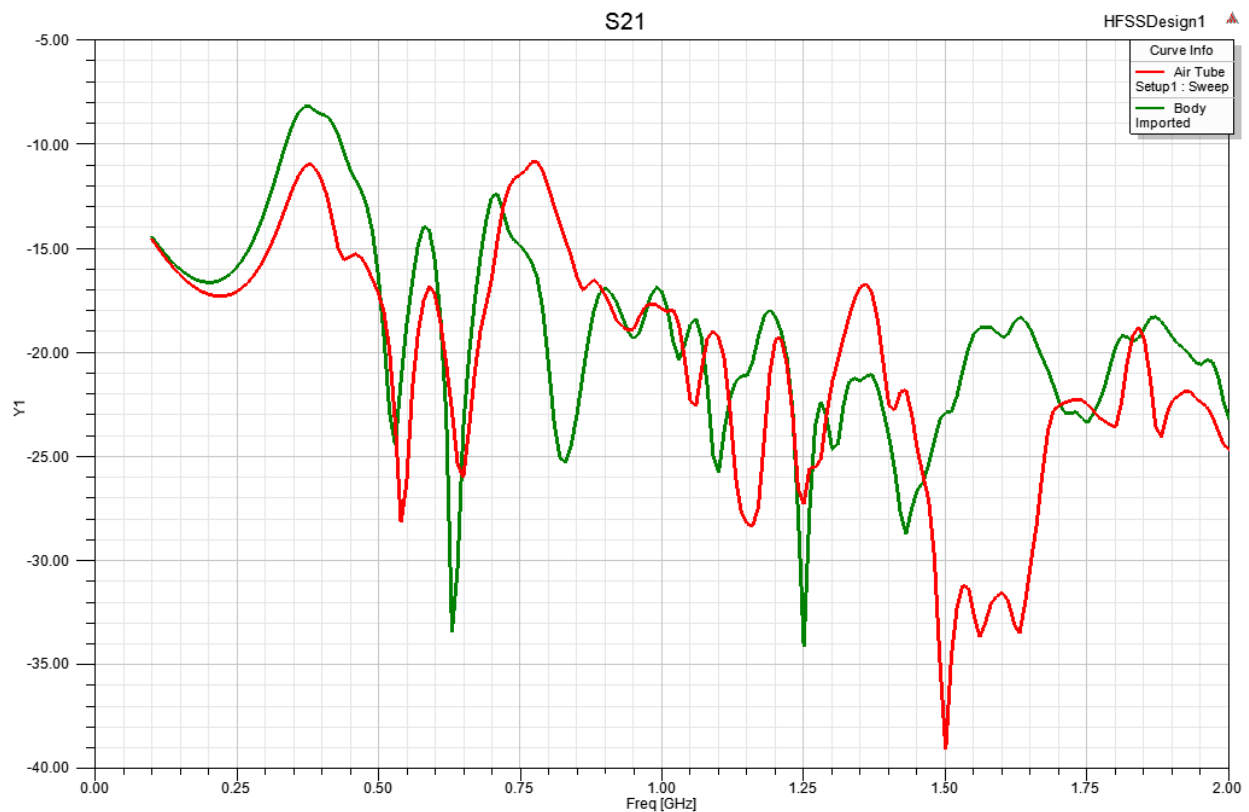


Figure 24: Ansys Simulation of Experimental Device

It was theorized that this was due to the dielectric effect of the muscle and bone tissue on the RF radiation. It was hoped that a significant difference could be seen when one compared the results of the S21 antenna transmission parameter from a healthy limb to one affected with osteoporosis. A noticeable change in the S21 resonances was seen in the simulations. The resonances shifted to the right, especially at higher frequencies with an osteoporotic bone compared to healthy bone as seen below.



**Figure 25: Ansys HFSS Results - Muscle Vs. Osteoporotic Bone**

### III. Printed Circuit Board (PCB) Fabrication

For this part of the project, we again decided to print a PCB to support both the baluns for the second version of the antenna, and for the third iteration of this section of the project, the antennas themselves. We once more used the toner-acid backmasking process and *Ultiboard* to fabricate the PCBs. This time though the requirements were a little different, instead of simply creating a circuit that would be hooked up to a power supply, multimeter, and oscilloscope we needed a more complete set-up. What we designed is a system of systems, which includes the balun, its wiring, and a means to attach it to the antenna and the medical phantom. We initially used a Dyson balun to match the antenna to the network analyzer, before moving onto a 180° power splitter. The Dyson balun was a purely mechanical design where the shields of the two feed lines are soldered together; the 180° power splitter was mounted on a PCB. The designs can be seen below:

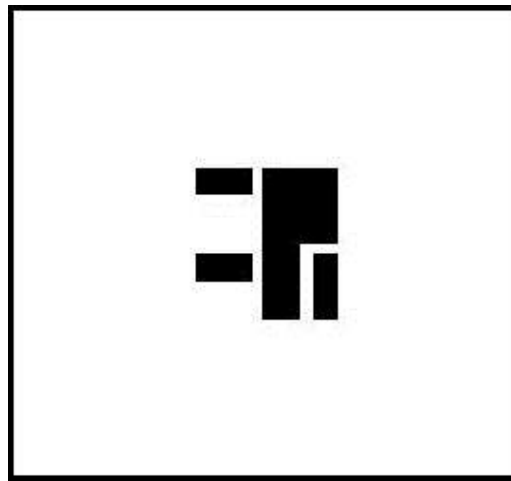


Figure 26: First Balun PCB Design

As you can see, the original design for the second version was a fairly simple layout that only included the power splitter itself, with enough pad space left over to attach the SMA coaxial cable and wiring for the antenna harness. For the third iteration we printed the 180° balun and the antenna, which is essentially a field probe being an electrically small dipole, on the same PCB. The design can be seen below:

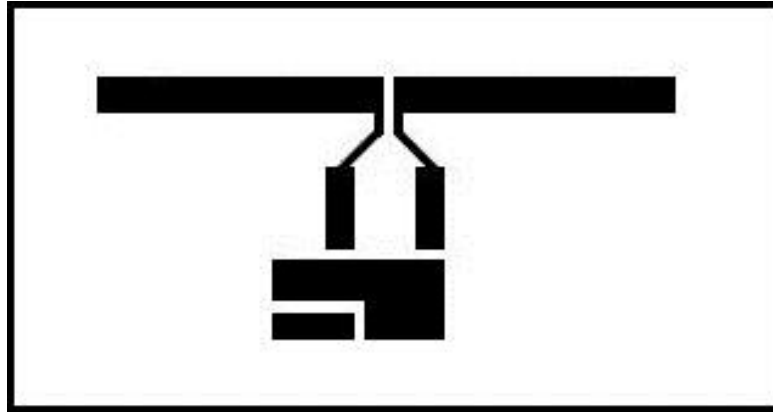


Figure 27: Balun and Antenna PCB Mask

What we are ultimately trying to accomplish with these PCBs is a “balun” or device to match a balanced line to an unbalanced line. Essentially, the impedance of the antennas we are using is extremely tiny, with a small amount of resistance, inductance, and capacitance, with most of the impedance resulting from inductance. The network analyzer expects fifty ohms of impedance to correctly analyze the antenna parameters, and we have to somehow match the antenna with the network analyzer. To do this we use a power splitter, this device has a number of toroid-wound transformers inside that match the electrical parameters of the antenna with the network analyzer. The power splitter also shifts the phase of the transmitted signals 180 degrees out of phase with respect to each other; this ultimately causes the current running through the antenna to rotate in the same direction. The concept for a balun can be seen below:

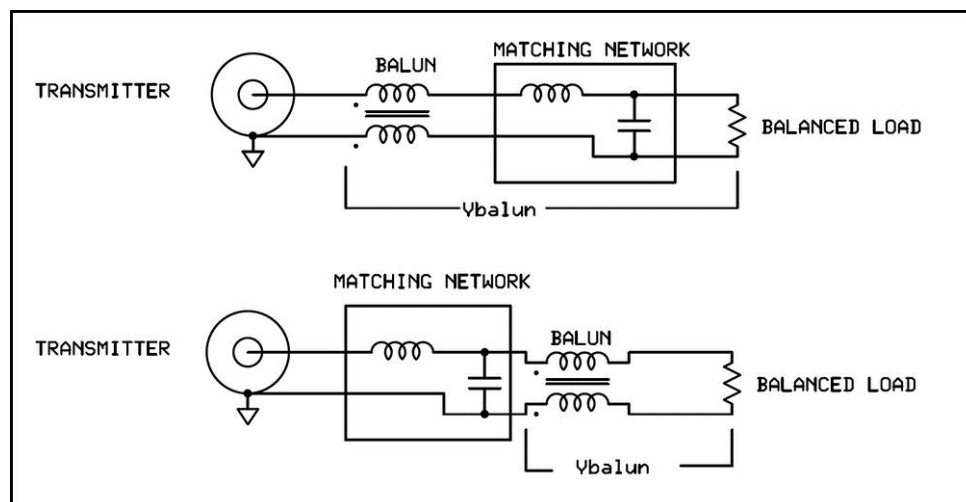


Figure 28: Concept of the Balun

## IV. Results

### IV-i. First Iteration

Our first practical implementation used a one third inch thick four inch wide Plexiglas tube with the antennas mounted on the outside. We positioned the feed as close together as possible on the side where the antennas are closest as well, thus hopefully creating the highest current density possible. We also fabricated a method of testing for osteoporotic bone as compared to healthy tissue; it was simply a one inch diameter PVC tube with a plastic cap at the end that seals the tube. This simulated a hollow, air-filled bone, such as one afflicted with osteoporosis. The results can be seen below:

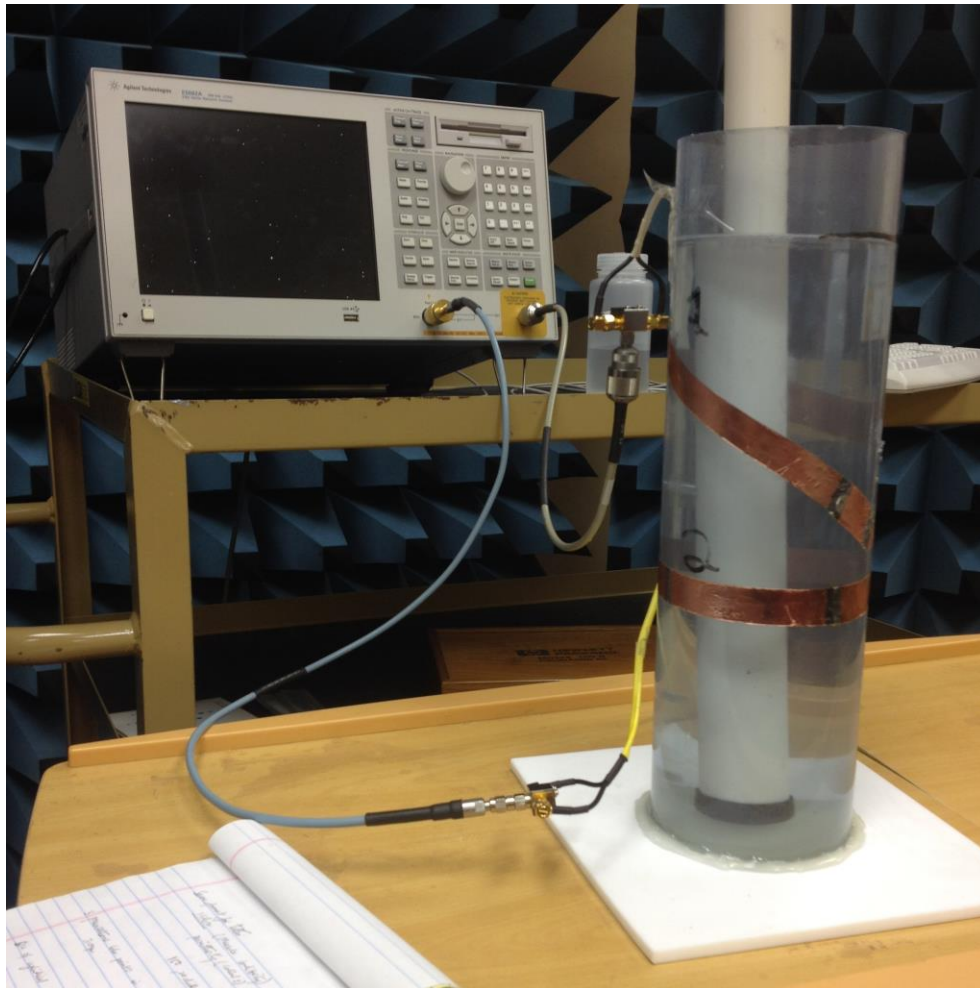
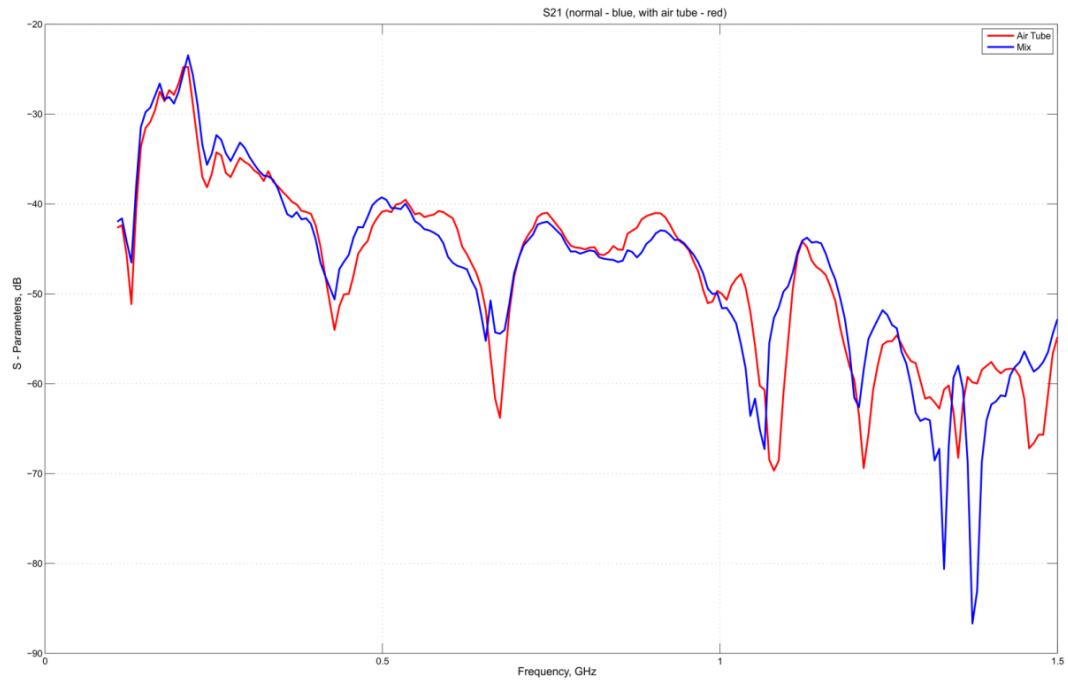
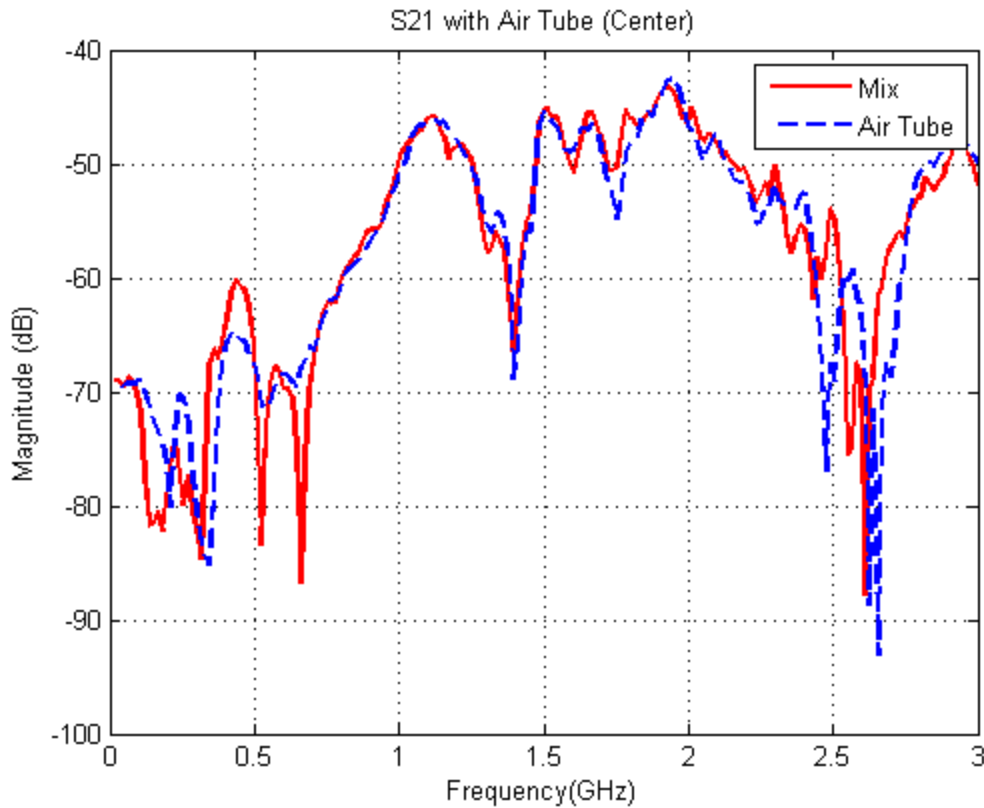


Figure 29: First Antenna Setup



**Figure 30: Original Cylinder Results**

Unfortunately it was observed that the results did not show a very large difference between the pure muscle simulation and the osteoporotic bone phantom. It was decided that the team would construct another device with the feeds as far apart as possible. The original simulations performed by Mr. Janakinadh Yanamadala had used the feeds positioned at the maximal distance point, essentially at the opposite side of the cylinder as ours in order to conform to HFSS standards. We had changed our feed position in order to maximize current density, which did not yield the expected results, so our team redesigned the medical phantom to more closely follow the Ansys simulations. This included moving the feeds to the maximal distance as well as mounting the antennas inside the device in direct intimate contact with the simulation fluid. We then again tested our device with the network analyzer, the product can be seen below:



**Figure 31: Second Experimental Setup Results**

As can be seen in the results, the outcome was not exactly clear cut. The S21 characteristics did indeed change, but S21 changed so quickly, and at such a minimal level that it was very difficult to obtain consistent effects from the antennas. With the bone simulator in place there was a slight shift, and we lost and gained resonances at 0.5 GHz and 2.4 GHz respectively. But these resonances shifted too much, even with high-gain averaging turned on. It was not possible to tell if one was shown the results with or without the tube if shown non-labeled results.

## IV-ii. Second Iteration

For the second iteration of the antenna design, we wanted replicate the conditions that would be experienced by the patient and the doctor to more closely than the previous device. We strove to make an antenna that would be adjustable for multiple leg widths and would be a single-use item that could be disposed of after one measurement.

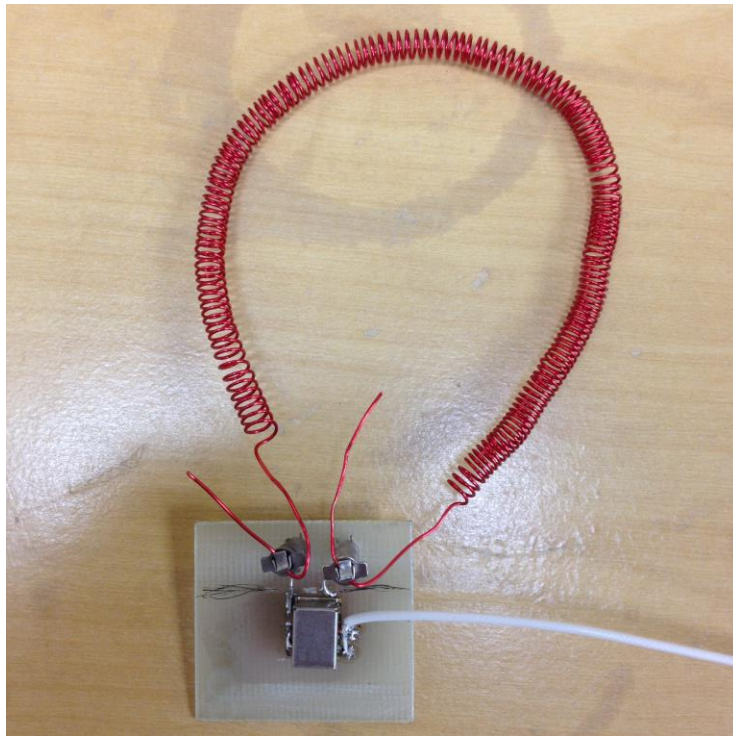


**Figure 32: Final Balun Design**

We settled upon using coils of wires that would stretch to accommodate the width of the leg of the patient. In order to reduce the amount of inductance that these coils would add, we planned on using the smallest possible coil diameter while still being able to wind them by hand to ease additional inductance and fabrication time respectively. Ten foot lengths of magnet wire seemed to be the best compromise between wire thickness, spring constant, and wire rebound. Since these antennas would only be used once, it was useful, but not necessary, for the antennas to rebound back to their original shape once stretched.



In order to correctly match these new antennas with the network analyzer, we again used our power splitter baluns. These matched the now highly inductive antennas to the fifty ohms necessary for the use of the network analyzer.



**Figure 33: Coil Antenna Setup**

Using the now correctly matched antennas we took the  $S_{21}$  measurements of the medical phantom with and without the osteoporotic bone replicating air tube. It was noted that there was a significant difference between the measurements with and without the air tube, but the resonances did not shift correctly. Some resonances grew, and others reduced in size, but they did not shift to the right. It was observed that we had now successfully mitigated the problems with the feed line. There was very little radiation being emitted from the feed lines, which allowed our measurements to reflect the actual conditions much better.

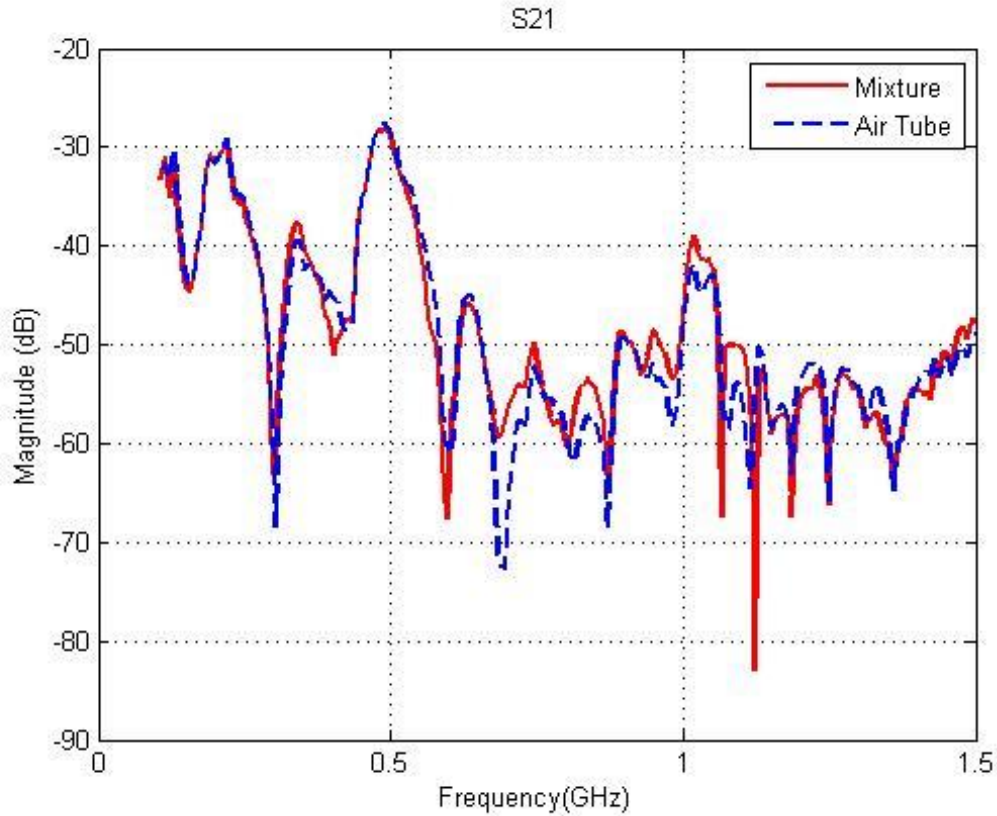


**Figure 34: Coil Antenna Results**

Though we had mitigated the issues with radiating feed lines, we still were not able to get very clear results from the actual experimental implementation. From these results, it can be fairly conclusively decided that the simulations do not correctly reflect reality. Even in the best simulations we were only seeing a one to two percent change in the resonance positions, this does not appear to bear out imperially. The small change in resonance patters appears to be lost in the background noise due to the environment and potentially lossy feed lines. One could potentially improve upon our experiments, especially by using better equipment, most notably the feed lines, baluns, and network analyzers.

## Conclusion

Distinguishing Osteoporotic bone from healthy bone is not an easy problem to solve. These three methods; Direct current sensor, Microwave sensor, and Infrared scattering sensor were built and tested to the best of our abilities in order to replace the current methods for osteoporosis detection. Our experiments produced some results that conformed to our simulations, but for the most part they were inconsistent. The three methods applied in this project are outstanding approaches for any future projects to take. Throughout the project, we overcame many challenges; such as selecting the right materials, faulty electronics, and incorrect simulations. Each of our approaches in this MQP served as a stepping stone from the previous method towards differentiating the measured electrical properties of the bone. We expect our final approach to implement a cross-coil antenna design [10] that will hopefully yield the most accurate measurements. This project served as a great learning experience and we were able to apply the different electrical properties of human bone in a useful and medically relevant manner.

## References

- [1] Bone Vitae. (2014). “Osteoporosis” [Online]. Available: <http://bonevitae.com/osteoporosis/>
- [2] C. Gabriel. “Compilation of the Dielectric Properties of Body Tissues at RF and Microwave Frequencies”, Report N.AL/OE-TR- 1996-0037, Occupational and Environmental Health Directorate, Radiofrequency Radiation Division, Brooks Air Force Base, Texas (USA), 1996.
- [3] C. Margaret, “Electrical Impedance Tomography,” *SIAM Review*, vol. 41, pp. 85-101, Mar. 1999.
- [4] D.I. Givens, “The Principles, Practices and Some Future Applications”, 10 ed. , Nutrition Research Reviews,
- [5] Gervain, Mehler, Werker, Nelson, Csibra, Lloyd-Fox, Shukla, Aslin “Near-infrared Spectroscopy: A report from the McDonnell infant”, 1 ed. , Elsevier Ltd.
- [6] G. M. Noetscher, J. Yanamadala, S. N. Makarov, A. Pascual-Leone, “Comparison of Cephalic and Extracerebral Montages for Transcranial Direct Current Stimulation – A Numerical Study,” *IEEE Transactions on Biomedical Engineering*, to appear, 2014.
- [7] G. M. Noetscher, S. N. Makarov, F. Scire-Scappuzzo, A. Pascual-Leone, “A Simple Absolute Estimate of Peak Eddy Currents Induced by TMS using the GR Model,” *IEEE Transactions on Magnetics*, vol. 49, no. 9, pp. 4999-5003, Sep. 2013.
- [8] International Osteoporosis Foundation. (2014). “Osteoporosis – Facts and Statistics” [Online]. Available: <http://www.iofbonehealth.org/facts-statistics#category-14http://bonevitae.com/osteoporosis/>
- [9] *ITIS Material Property Database*, Retrieved Oct. 2<sup>nd</sup> 2013 from <http://www.itis.ethz.ch/itis-for-health/tissue-properties/overview/>
- [10] J.M. Elloian, G. M. Noetscher, S. N. Makarov, A. Pascual-Leone, “Continuous Wave Simulations on the Propagation of Electromagnetic Fields Through the Human Head,” *IEEE Transactions on Biomedical Engineering*, to appear, 2014.

- [11] Kelly E. Hall, “Measurement of Tissue Oxygen Saturation Levels Using Portable Near-Infrared Spectroscopy in Clinically Healthy Dogs”, Veterinary Emergency and Critical Care Society.
- [12] M. Rafiei-Naeini and H McCann, “Low-Noise Current Excitation Sub-System for Medical EIT,” *Physiol. Meas.*, vol. 29, 2008, pp. S173–S184.
- [13] R. L. McIntosh and V. Anderson. A Comprehensive Tissue Properties Database Provided for the Thermal Assessment of a Human at Rest, *Biophysical Reviews and Letters*, vol. 5, no. 3, pp. 129-151, 2010.
- [14] R.H. Bayford, “Bioimpedance Tomography (Electrical Impedance Tomography),” *Annual Review of Biomedical Engineering*, vol. 8, pp. 63-91, Aug. 2006.
- [15] Strangman, Gary, “Non-invasive neuroimaging using near-infrared light”, *Biological Psychiatry*, vol. 52, pp. 679-693, Oct. 2002.
- [16] Texas Instruments, Application Report SNOA474A–January 2008–Revised April 2013 AN-1515 A Comprehensive Study of the Howland Current Pump.
- [17] Villringer, Arno, “Non-invasive optical spectroscopy and imaging of human brain function”, *Trends in Neurosciences*, vol. 20, pp. 435-442, Oct. 1997.
- [18] Yanamadala, Elloian, Ruzzi, Maliye, Makarov, “Non-Invasive Detection/Monitoring of Osteoporosis”, Unpublished.
- [19] Y. Gimm, “General Method of Formulating the Human Tissue Simulant Liquid for SAR Measurement” *EMC 2004-Sendai*, 3B2-1, Aug. 2004.

## Appendix A – MATLAB Code to View Network Analyzer Results

```
% Written by Jeffrey Elloian
% Modified by Michael Ruzzi

close all

temp=csvread('File Name Here.CSV',4,0);
f=temp(:,1);
Smag1=temp(:,2);

temp=csvread('File Name Here.CSV',4,0);
Smag2=temp(:,2);

% temp=csvread('File Name Here.CSV',4,0);
% f=temp(:,1);
% Smag3=temp(:,2);

figure(1)
plot(f./1e9,Smag1,'Color','r','Linewidth',2)
hold on
plot(f./1e9,Smag2,'Color','b','Linewidth',2,'Linestyle','--')

% plot(f./1e9,Smag3,'Color','g','Linewidth',2,'Linestyle',':')

xlabel('Frequency(GHz)')
ylabel('Magnitude (dB)')
hold off
title('S21')
legend('Mixture','Air Tube')
grid on
```

## Appendix B – MATLAB Code for Tissue Frequency Parameters

```
% Written by Professor Sergey N. Makarov
% Modified by Saili Maliye
% Reviewed by Jeffrey Elloian

clear all
close all
%% EM constants
eps0      = 8.85418782e-012;    % dielectric permittivity of vacuum(~air)
mu0       = 1.25663706e-006;    % magnetic permeability of vacuum(~air)
c0        = 1/sqrt(eps0*mu0);   % speed of light in vacuum(~air)
eta0      = sqrt(mu0/eps0);     % vacuum/air impedance, ~377 ohms

%% Open data files
% red
fileID     = fopen('BoneCortical.txt', 'r');
A          = fscanf(fileID, '%f %f %f', [3 inf]);
freq       = A(:, 1);
epsBO      = A(:, 2);
sigBO      = A(:, 3);
fclose(fileID);

% green
fileID     = fopen('BoneCancellous.txt', 'r');
A          = fscanf(fileID, '%f %f %f', [3 inf]);
freq       = A(:, 1);
epsBC      = A(:, 2);
sigBC      = A(:, 3);
fclose(fileID);

% yellow
fileID     = fopen('BoneMarrowYellow.txt', 'r');
A          = fscanf(fileID, '%f %f %f', [3 inf]);
freq       = A(:, 1);
epsBM      = A(:, 2);
sigBM      = A(:, 3);
fclose(fileID);

% blue
fileID     = fopen('FatAverage.txt', 'r');
A          = fscanf(fileID, '%f %f %f', [3 inf]);
freq       = A(:, 1);
epsFA      = A(:, 2);
sigFA      = A(:, 3);
fclose(fileID);

% magenta
fileID     = fopen('Muscle.txt', 'r');
A          = fscanf(fileID, '%f %f %f', [3 inf]);
freq       = A(:, 1);
epsMU      = A(:, 2);
sigMU      = A(:, 3);
fclose(fileID);
```

```

% lambdas
lamda0=(c0./freq); %in air
lamBO=(c0./freq)./sqrt(epsBO);
lamBM=(c0./freq)./sqrt(epsBM);
lamBC=(c0./freq)./sqrt(epsBC);
lamFA=(c0./freq)./sqrt(epsFA);
lamMU=(c0./freq)./sqrt(epsMU);

freq=freq/1e6; %convert frequency to MHz
fontsize=12;
a = figure;
semilogx(freq, epsBO, 'r', 'LineWidth', 3); hold on;
semilogx(freq, epsBM, 'y', 'LineWidth', 3); hold on;
semilogx(freq, epsBC, 'g', 'LineWidth', 3); hold on;
semilogx(freq, epsFA, '--b', 'LineWidth', 1.5); hold on;
semilogx(freq, epsMU, '--m', 'LineWidth', 1.5); hold on;
grid on;
axis([100,1500,0,80])
title('Frequency Dependence of \epsilon_r for Selected
Tissues','fontsize',fontsize)
xlabel('Frequency (MHz)','fontsize',fontsize)
ylabel('Dielectric Constant, \epsilon_r','fontsize',fontsize)
t1=legend('Cortical Bone','Yellow Bone Marrow','Cancellous
Bone','Fat','Muscle');
set(t1,'fontsize',fontsize)

b = figure;
title('tissue conductivity, S/m')
semilogx(freq, sigBO, 'r', 'LineWidth', 3); hold on;
semilogx(freq, sigBM, 'y', 'LineWidth', 3); hold on;
semilogx(freq, sigBC, 'g', 'LineWidth', 3); hold on;
semilogx(freq, sigFA, '--b', 'LineWidth', 1.5); hold on;
semilogx(freq, sigMU, '--m', 'LineWidth', 1.5); hold on;
grid on;
axis([100,1500,0,1.5])
title('Frequency Dependence of \sigma for Selected
Tissues','fontsize',fontsize)
xlabel('Frequency (MHz)','fontsize',fontsize)
ylabel('Conductivity, \sigma, (S/m)','fontsize',fontsize)
t2=legend('Cortical Bone','Yellow Bone Marrow','Cancellous
Bone','Fat','Muscle');
set(t2,'fontsize',fontsize)
set(t2,'Location','NorthWest')
return;

%% Differences
diffeps=abs((epsBC-epsBM)./epsBC)*100;
diffsig=abs((sigBC-sigBM)./sigBC)*100;

c = figure;
semilogx(freq, diffeps, 'r', 'LineWidth', 3);
grid on;
axis([100,1500,40,100])

```



```

title('Difference in \epsilon_r between Cancellous Bone and Yellow Bone
Marrow','fontsize',fontsize)
xlabel ('Frequency (MHz)','fontsize',fontsize)
ylabel('% Difference in \epsilon_r','fontsize',fontsize)

d = figure;
semilogx(freq, diffsig, 'r', 'LineWidth', 3);
grid on;
axis([100,1500,40,100])
title('Difference in \sigma between Cancellous Bone and Yellow Bone
Marrow','fontsize',fontsize)
xlabel ('Frequency (MHz)','fontsize',fontsize)
ylabel('% Difference in \sigma','fontsize',fontsize)

%% Plot Wavelengths

e = figure;
loglog(freq, lamBO, 'r', 'LineWidth', 3); hold on;
loglog(freq, lamBM, 'y', 'LineWidth', 3); hold on;
loglog(freq, lamBC, 'g', 'LineWidth', 3); hold on;
loglog(freq, lamFA, '--b', 'LineWidth', 1.5); hold on;
loglog(freq, lamMU, '--m', 'LineWidth', 1.5); hold on;
loglog(freq, lamda0, '--k', 'LineWidth', 1.5); hold on;
grid on;
axis([100,1500,0,100])
title('Wavelength in Selected Tissues','fontsize',fontsize)
xlabel ('Frequency (MHz)','fontsize',fontsize)
ylabel('Wavelength, \lambda (m)','fontsize',fontsize)
t3=legend('Cortical Bone','Yellow Bone Marrow','Cancellous
Bone','Fat','Muscle','Air');
set(t3,'fontsize',fontsize)

```